Bull Volcanol (2007) 69:825–845
DOI 10.1007/s00445-006-0111-4

RESEARCH ARTICLE

Multiple origins of obsidian pyroclasts and implications for changes in the dynamics of the 1300 B.P. eruption of Newberry Volcano, USA

A. C. Rust · K. V. Cashman

Received: 12 October 2005 / Accepted: 22 November 2006 / Published online: 10 January 2007

Abstract The pyroclastic deposits of the 1300 B.P. eruption of Newberry Volcano, OR, USA, contain minor amounts of obsidian (1–6 wt.%). The volatile (H_2O and CO_2) contents and textures of these clasts vary considerably. FTIR measurements of H_2O in obsidian pyroclasts range from 0.1 to 1.5 wt.% indicating equilibration pressures ≤20 MPa. CO_2 contents are low (<10 ppm) except in clasts that also contain xenolith powder that provided a local CO_2 source. Obsidian clasts exhibit a range of color and textural types that changed in relative proportion as the eruption progressed. Together these data indicate that there were multiple origins of obsidian and that the dominant source changed during the eruption. Early in the eruption, obsidian was almost entirely black or grey (microlite-bearing) and probably derived from dikes or wall rock fractures filled with vanguard magma or tuffisite that, together with wall rocks, were eroded and incorporated into the eruption column as the vent widened. Later in the eruption, following a brief cessation of activity, the proportion of obsidian to wallrock lithic clasts increased and new types of obsidian dominated, types that represent remnants of a shallow conduit plug, welded fallback material from within the conduit, and sheared and degassed magma from near the conduit walls. Analysis of bubble shapes preserved within obsidian indicates that shear stresses and shear rates varied by over two orders of magnitude, with maxima of 88 kPa and $10^{-2.3}$ s^{-1}, respectively, based on an assumed magma temperature of 850°C. Furthermore, the highest shear rates and stresses, and the shortest flow times (10–20 min), are preserved in clasts that also contain wall rock. The longest deformation times (5 and 8 h) correspond to two microlite-rich clasts, suggesting that the higher microlite content results from slower ascent rates and/or longer magma residence times at shallow levels. Differences between obsidian pyroclasts from the Newberry eruption and those of the Mono Craters may relate to the nature of the conduit feeding the two events. From this comparison, we conclude that obsidian can provide information on time scales and mechanisms of pre-fragmentation magma ascent.

Keywords Bubbles · Newberry · Magma · Microlites · Obsidian · Pyroclastic · Shear · Volatiles

Editorial responsibility: J. McPhie

A. C. Rust (✉)
Department of Earth Sciences,
University of Bristol,
Wills Memorial Building, Queens Road,
Bristol BS8 1RJ, UK
e-mail: alison.rust@bristol.ac.uk

K. V. Cashman
Department of Geological Sciences,
1272 University of Oregon,
Eugene, OR 97403, USA

Introduction

Obsidian clasts may be a minor component in deposits from explosive rhyolite eruptions of all magnitudes and styles. As the low vesicularity of obsidian makes it ideal for CO_2 and H_2O analysis, these data have been used to address syn-eruptive degassing and fragmentation conditions of both Plinian and subplinian eruptions (Bursik 1993; Dunbar and Kyle 1992; Newman et al. 1988; Taylor 1991; Taylor et al. 1983). However, questions remain about both the

degassing process responsible for obsidian formation and the physical conditions required to first form, and then erupt, dense glassy clasts of variable H_2O content, as illustrated by the several models that seek to explain obsidian formation during the well studied 1340 A.D. Mono Craters eruption (Bursik 1993; Gonnermann and Manga 2005; Newman et al. 1988; Rust et al. 2004). Degassing questions revolve around the observation that although the low porosity of obsidian requires that gas be lost from the system, the CO_2 contents are too high to result from end member open-system degassing. These high CO_2 contents led Newman et al. (1988) to model obsidian degassing using closed-system conditions, despite the contradiction posed by the paucity of retained bubbles. More recent studies address this discrepancy by invoking either buffering due to fluxing vapor (Rust et al. 2004) or non-equilibrium vesiculation (Gonnermann and Manga 2005). Suggested obsidian formation processes include densification in a zone of high shear rates at conduit margins (Newman et al. 1988; Rust et al. 2004; Stasiuk et al. 1996), unvesiculated pockets of melt (Newman et al. 1988) or water quenching of magma within the conduit at levels of aquifers (Bursik 1993). Determining the origin of obsidian in pyroclastic deposits, including whether it is juvenile or accessory wall rock, is critical for incorporation of obsidian data in eruptive models (e.g. Bursik 1993).

Here we examine both the degassing and fragmentation history of obsidian in pyroclastic deposits from the 1300 B.P. rhyolite eruption of Newberry Volcano, Oregon, using a combined strategy of volatile measurements and textural analysis. Although also subplinian, this event, with a fall deposit followed by a pyroclastic flow deposit and obsidian lava flow from a single vent, has a much simpler eruptive history than the 1340 AD Mono Craters sequence and thus provides a useful perspective from which to view broader questions of obsidian formation. We show that H_2O and CO_2 contents of the Newberry obsidian pyroclasts have ranges and temporal patterns that are quite different from those of Mono Craters. Moreover, we demonstrate that classification of obsidian textures allows variations in magma ascent history and vent architecture to be assessed throughout the course of an eruption. We show that there are multiple origins of obsidian and that the dominant obsidian source changed during the course of the eruption.

While we cannot rule out that some of the obsidian clasts are fragments of rhyolite wallrock unrelated to the eruption, there is considerable evidence from componentry, obsidian microtextures, major element glass composition and glass volatile contents that most of the obsidian pyroclasts are juvenile. Our analyses of physical and chemical properties of obsidian pyroclasts allow us to constrain the source depths, degassing processes and deformation history of the ascending magma.

The 1300 B.P. Newberry Volcano eruption

Newberry Volcano is centered 60 km east of the Cascade volcanic arc in central Oregon, USA (MacLeod and Sherrod 1988). Rhyolite and dacite lavas typically erupt near the summit caldera, whereas more mafic lavas erupt on the flanks. The volcano has produced at least 40 rhyolitic or dacitic pyroclastic deposits in the last 500,000 years (Kuehn 2002), with four distinct rhyolitic eruption periods in the last 10,000 years. The most recent, called the Big Obsidian Eruptive Period, occurred about 1300 B.P. (Kuehn 2002; MacLeod and Sherrod 1988).

The Big Obsidian Eruptive Period began with an explosive eruption that produced a widespread fall deposit (Newberry Pumice), followed by a small pyroclastic flow (Paulina Lake Ash Flow) and emplacement of an obsidian lava flow (Big Obsidian Flow; Fig. 1). These three phases are compositionally indistinguishable and appear to have erupted from the same vent (MacLeod and Sherrod 1988). A reworked ash layer that underlies the Newberry Pumice may also be part of the Big Obsidian Eruptive Period, suggesting that there was minor explosive activity prior to the climactic eruption (Kuehn 2002). The total erupted volume is about 0.2 km^3 dense rock equivalent (DRE) divided approximately equally between the obsidian lava and pyroclastic fall deposits, with only 0.002 km^3 DRE in the pyroclastic flow deposit (MacLeod and Sherrod 1988). The total tephra volume of 0.1 km^3 is typical of deposits from supblinian eruptions (VEI=4).

We focus on the Newberry Pumice (NP) pyroclastic fall deposit, which has a maximum thickness of ~8 m and forms a narrow lobe oriented slightly north of east (Fig. 1b), indicating a westerly wind throughout the eruption. Applying the method of Carey and Sparks (1986); Gardner et al. (1998) estimated that the climactic eruption column was 21 km high (cf. 25 km, Kuehn 2002) and decreased to 18 km by midway through deposition of the NP. This column height range spans that commonly used to distinguish Plinian from subplinian eruptions (Cioni et al. 2000). However, the elongate isopachs (Fig. 1b) suggest the peak wind speed was well in excess of 50 m/s, which is more than two standard deviations faster than measured in typical modern wind profiles for the area (Carey and Sparks 1986; Kuehn 2002). As subplinian eruption columns are often bent over by even moderate winds (Bursik 2001), we suggest that the calculated column heights may be overestimates and we prefer a subplinian classification for the deposit consistent with the small volume of tephra.

The juvenile component of the NP is dominantly white pumice with lesser amounts of grey pumice, obsidian, and aggregate pumice clasts containing oxidized (pink) ash between non-oxidized pumice fragments. After white pum-

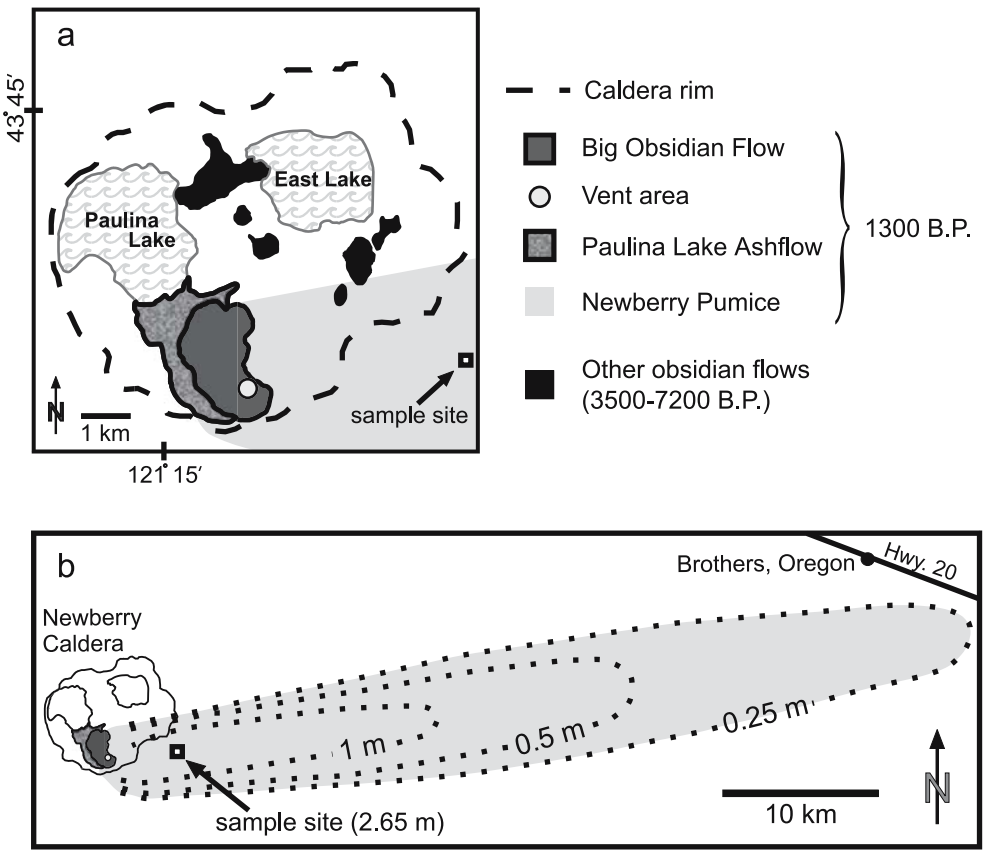

Fig. 1 **a** Map of Newberry Caldera, central Oregon, showing deposits of the 1300 BP Big Obsidian eruptive period and other recent obsidian flows. **b** Isopachs of the Newberry Pumice, the 1300 B.P. fall deposit, based on Jensen and Chitwood (2000). The samples of this deposit were collected at the marked location. See Kuehn (2002) for a photograph of the outcrop sampled (#97-5)

ice, the most abundant clasts are lithic fragments of fresh and altered volcanic rocks including reworked volcaniclastic rocks. The NP has been divided into lower and upper sections based on a rapid decrease in average and maximum clast size from the lower to the upper portions of the deposit (Kuehn 2002). This distinction is clear at sites 10–30 km from the vent; however, the boundary is commonly not evident at more proximal sites where clast sizes are more variable and the upper section contains up to seven ash layers (Kuehn 2002). Although these ash layers are observed within the NP as far as 17 km from the vent, only the lowermost ash, which is about 1 cm thick in proximal areas, is distinct enough to be easily correlated between sites. The ash layers have been interpreted as surge or co-surge ash fall deposits by Gardner et al. (1998), although Kuehn (2002) also considers pauses in eruptive activity, drastic column height reduction, and phreatomagmatic activity to be viable interpretations. As our study of proportions, textures and volatile contents of obsidian pyroclasts indicates that the lowest ash layer has a different origin from higher ash layers and that this lowermost ash marks an important change in the dynamics of the eruption, we refer to units below and above this ash layer as the Lower NP and Upper NP, respectively (Fig. 2). In sections where comparison is possible, our division of the NP is stratigraphically higher than the division mapped by Kuehn (2002).

Samples, methods and assumptions

The primary focus of this study is pyroclastic obsidian, which is ubiquitous but comprises at most a few percent of the mass of the NP and the Paulina Lake Ash Flow deposit. We assume that the obsidian is juvenile, which is consistent with the major-element glass composition: all eleven obsidian pyroclasts we analysed match the composition of pumice and glass shards from the NP, which is distinct from products of other Holocene silicic eruptions from Newberry Volcano (Kuehn 2002; Kuehn and Foit 2006).

We sampled the NP at site 97-5 of Kuehn (2002), which is 4.3 km from the vent, slightly north of the dispersal axis (Fig. 1). The deposit is 2.65 m thick at this location, where we collected 12 bulk samples at different stratigraphic heights, each over a stratigraphic interval of 10 cm (Fig. 2). Samples were cleaned, dried and sieved to the 1 mm size fraction. Lithic and obsidian clasts $\geq$ 6 and 1 mm, respectively, were separated from the pumice based on visual inspection. For bulk samples with large fractions of ash and small lapilli, obsidian was separated only from a sample split. Obsidian pyroclasts that contain fragments of wall rock (xenoliths) were classified as obsidian, and only discrete fragments of wall rock were classified as lithic clasts. We use the term "xenolith" as a general term for all pieces of wallrock in obsidian regardless of size. Generally

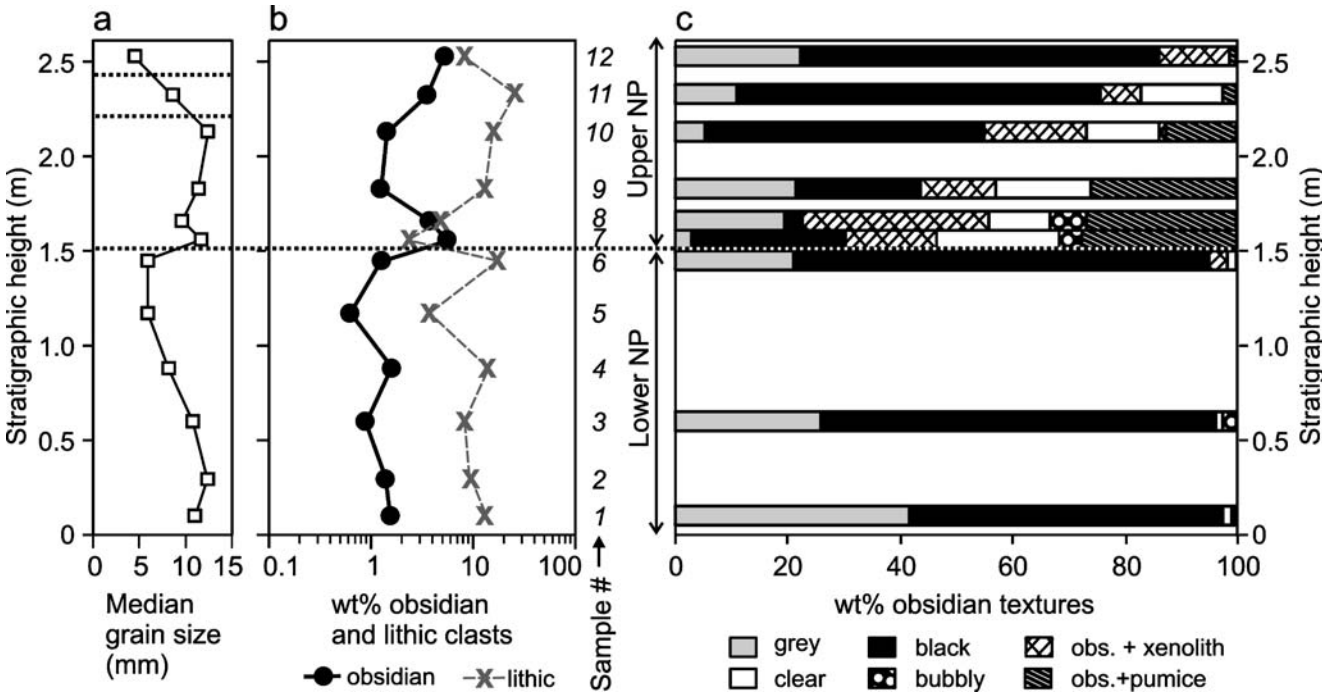

Fig. 2 Variations in median grain size and relative proportion of lithic clasts, obsidian, and obsidian types in the stratigraphic section (site shown in Fig. 1). The Newberry Pumice is divided into Upper NP and Lower NP, separated by a distinct ash bed indicated with a *dotted line*. **a** Variations in the grain size for which half of the deposit by mass is composed of smaller fragments (Mdφ). **b** Variations in proportion of the deposit by mass that is obsidian clasts >2 mm and lithic clasts >6 mm. The logarithmic scale for percentage of obsidian and lithic clasts shows that there is generally an order of magnitude more lithic than obsidian clasts. **c** Variations in obsidian textures determined visually

the xenoliths are extremely fine (submicron to micron) and we use the term "xenolith powder" when single particles cannot be discerned visually.

Obsidian clasts from all bulk samples except 2 and 4 (Fig. 2) were sorted visually by texture for FTIR analysis. We analysed 2–4 mm clasts from the lowermost bulk sample (sample 1 in Fig. 2) and 4–8 mm clasts from all other samples. Two large (>1 cm) xenolith-bearing obsidian clasts from bulk sample 7 were ground and polished to examine variations in texture and volatile content at a larger scale. Clasts were subdivided into six types: (1) grey (containing silicate microlites), (2) black, (3) clear glass, (4) clear glass with macroscopic xenoliths or macroscopic opaque bands of clear glass with dispersed xenolith powder, (5) clear glass with numerous macroscopic bubbles but not enough to appear white like pumice, and (6) obsidian mingled with white pumiceous glass (Fig. 2c). Black obsidian is most abundant and there are multiple causes of the dark color (microlites, dark brown glass, xenolith powder, and/or a xenolith core). With the aid of a microscope, black obsidian clasts prepared for FTIR analysis were divided into those with and without xenoliths. Clasts from the Lower NP (bulk samples 1, 3 and 6) as well as from the base of the Upper NP (bulk sample 7) were further sorted on the basis of glass color, microlite content and bubble content.

FTIR

A total of 411 spots on 300 obsidian pyroclasts from the Paulina Lake Ash Flow deposit and ten stratigraphic levels in the NP were analyzed for water and carbon dioxide by Fourier transform infrared spectroscopy (FTIR). The obsidian clasts were ground and polished to form tablets between 54 and 978 μm thick (median 549 μm; Rust 2003) with parallel surfaces. Clasts with relatively high crystal or dispersed xenolith powder contents were ground thinner than other samples to ensure adequate transmission of IR radiation. Most grey obsidian clasts have water contents less than 0.25 wt.% and relatively high silicate microlite contents (>1%). The consistently low H_2O contents of these clasts in the Lower NP was assumed to hold for similar clasts in the Upper NP, thus we did not analyze clasts of this type stratigraphically above bulk sample 7.

All FTIR analyses were done on a Thermo Nicolet Nexus 670 spectrophotometer with attached Continuum IR microscope at the University of Oregon. Transmission IR spectra were acquired using a square or rectangular aperture, usually 200 by 200 μm except when reduced to avoid bubbles or xenoliths. Typically 256 or 512 scans were collected, although some less transparent samples required more scans to improve the signal to noise ratio. Molecular CO_2, hydroxyl (OH), and molecular H_2O

(H_2Om), dissolved in the glass were calculated from absorbance spectra peaks at 2,350, 4,500, and 5,200 cm^{-1}, respectively. If the 4,520 and 5,240 cm^{-1} peaks were too small, as was typical for samples with less than 0.25 wt.% H_2O, then the 3,500 cm^{-1} peak was used to determine the total water content. The extinction coefficients and references are listed in Table 1. Sample thicknesses were measured with a digital micrometer with 1 μm resolution; density was calculated from glass composition (Kuehn 2002) using the formulation of Lange and Carmichael (1987, 1990). Although detection limits varied with sample thickness, glass clarity and crystal content, CO_2 detection limits were typically ~1 ppm. This limit is much lower than in most melt inclusion studies, which are constrained by small FTIR apertures and thin samples.

Bubble geometry

Of the obsidian clasts polished for FTIR spectroscopy, we selected 12 for measurements of bubble shapes and sizes to assess flow parameters (Rust et al. 2003). All clasts are from the bulk sample 7 from the base of Upper NP, which contains a relatively high proportion of obsidian clasts. For geometric measurements, bubbles must be symmetrically deformed and the longest dimension of the most deformed bubbles must lie approximately parallel to the polished surfaces. The 12 obsidian clasts chosen (Fig. 3) include the six texture types from visual sorting (Fig. 2c). To measure bubble dimensions, the polished obsidian was placed on a glass slide centered on the stage of an optical microscope. The longest bubbles in the obsidian were rotated to horizontal by slightly tilting the glass slide, which was then held in place with modeling putty.

Flow type (simple or pure shear) can be assessed from the shapes as a function of size of highly deformed larger bubbles or from bubble orientations (Rust et al. 2003), which are parallel to the flow direction in pure shear but vary systematically with bubble shape in simple shear. The small dimensions of the obsidian pyroclasts in this study preclude quantitative assessment of flow type by bubble shape. Instead we make qualitative assessments of flow type from the orientations of bubbles relative to the local flow direction as determined by orientations of microlites or the most deformed bubbles.

Shear rates and shear stresses are determined from the dimensions of slightly deformed bubbles as a function of their size. The calculation begins with linear fits to D vs. r data for bubbles with $D<0.5$, where r is the radius of a sphere of the same volume as the bubble and D is a dimensionless bubble deformation parameter defined as

$$D = (l - b)/(l + b), \tag{1}$$

where l and b are the semi-major and semi-minor axes of the deformed bubble. The linear D–r fits, together with theoretical D–Ca equations, give the relationship between bubble size (r) and capillary number (Ca), a dimensionless parameter that indicates the relative importance of viscous to surface tension stresses acting on the bubbles and defined as

$$\mathrm{Ca} = \frac{r\dot{\gamma}\mu}{\Gamma}, \tag{2}$$

where $\dot{\gamma}$ is shear rate, μ is melt viscosity and Γ is surface tension. Determining shear stress ($\mu\dot{\gamma}$) requires an estimate of Γ; calculating shear rate also requires an additional estimate of μ.

Effect of melt temperature

Temperature affects the viscosity of silicate melt as well as the diffusivities and solubilities of H_2O and CO_2. Therefore uncertainty in temperature contributes to errors in estimates of saturation pressures, shear rates and time scales of flow, welding, and volatile element diffusion. The dearth of crystals in NP pyroclasts precludes crystal geothermometry but suggests proximity to the liquidus temperature prior to ascent and microlite growth. Hence, we take a liquidus temperature of 1,053°C for the NP rhyolite composition (Kuehn 2002) with the maximum H_2O measured in NP obsidian pyroclasts obsidian, 100 MPa, and QFM +1 to be an upper bound for the melt temperature (e.g. Boudreau 1999). However, according to the Pele program (Boudreau 1999), under these conditions the liquidus phase is Fe–Ti oxide and the first silicate phase (plagioclase) should not crystallize until about 900°C whereas pyroxene, the dominant microlite phase, is not predicted to crystallize before the end of simulation at 700°C. Melt temperatures of <1,050°C are also inferred from pyroxenes in quenched mafic enclaves within the associated Big Obsidian flow (Lindsley and Spencer 1982; Linneman and Myers 1990). Furthermore, Fe–Ti oxide temperatures of mafic inclusions decrease with coarsening average grain size and those of

Table 1 The extinction coefficients (ε) used to calculate water and carbon dioxide contents dissolved in glass, and the wave numbers of the corresponding absorbance peaks

Species	Wavenumber (cm^{-1})	ε (L mol^{-1} cm^{-1})	Reference
CO_2	2,350	1,077	Blank 1993
H_2O	3,500	80	Ihinger et al. 1994
H_2Om	5,239	1.86	Ihinger et al. 1994
OH^-	4,520	1.5	Ihinger et al. 1994

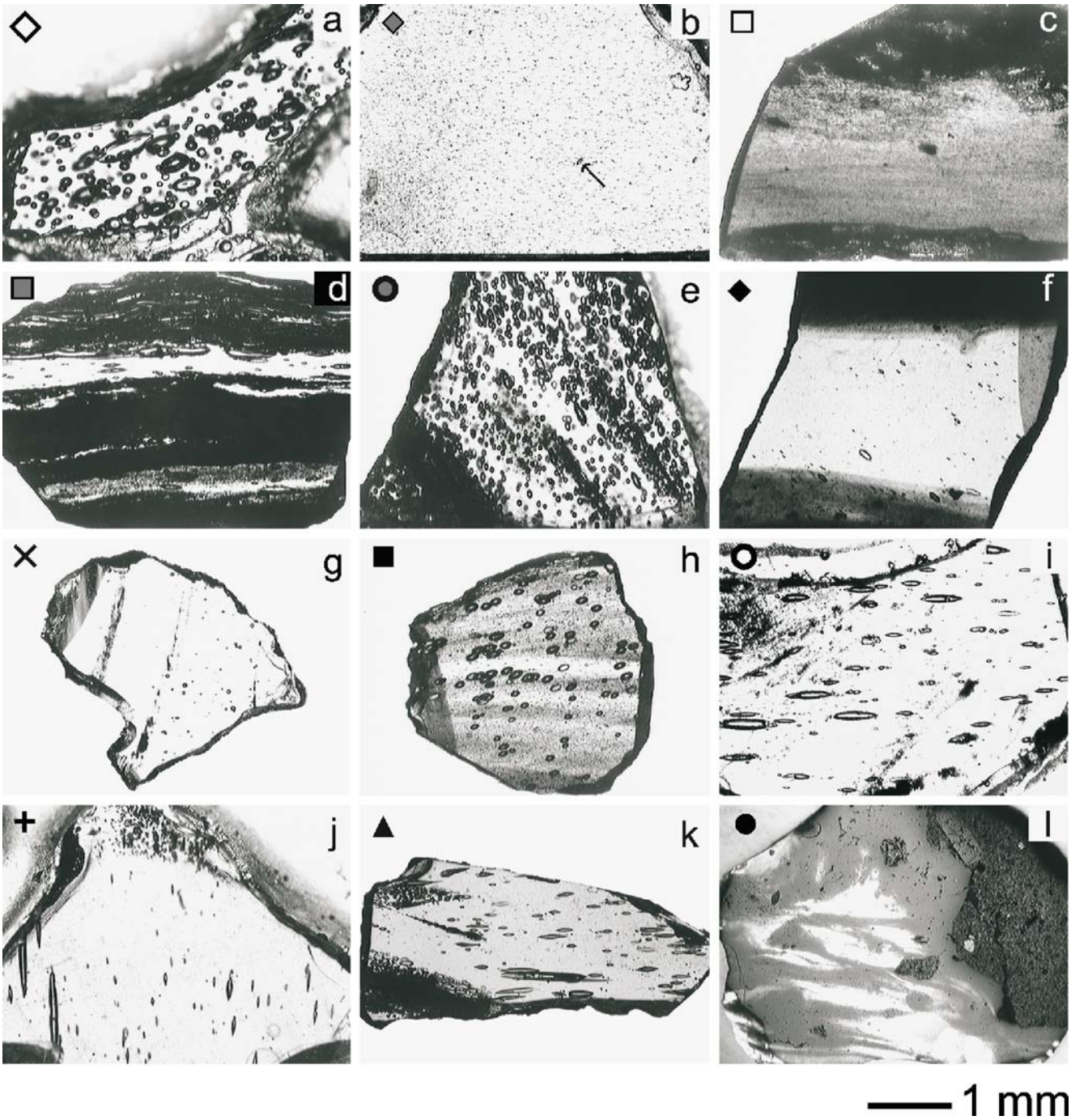

the coarsest inclusions cluster at 850°C (Linneman and Myers 1990). Although the crystallization temperature of the coarse mafic inclusions does not necessarily indicate the rhyolite temperature, we assume 850°C for the rhyolite throughout this study as this temperature is both consistent with the available temperature constraints and within the range reported for other rhyolite magmas (e.g., Frost and Lindsley 1992).

Uncertainty in the melt temperature is the greatest potential source of error in shear rate calculations as well as in calculations of bubble deformation and viscous welding times. For example, a lower/higher temperature implies a more/less viscous melt, which in turn implies a smaller/greater shear rate for a given range of *D–r* characteristics. In particular, for 0.72 wt.% H_2O (clast c Fig. 3, Table 2) at 700, 800, 900 and 1,000°C the shear rate calculated assuming 850°C would be multiplied by about 0.008, 0.3, 4, and 300, respectively, thus illustrating that a temperature variation of 300°C produces a four order of magnitude variation in estimated shear rate. In contrast,

◀ **Fig. 3** Photomicrographs of the 12 clasts used for bubble shape analysis from bulk sample 7 (Fig. 2). The thicknesses of these doubly polished tablets vary from 360 to 970 μm and so the bubble and crystal contents appear greater than would be the case if they were as thin as standard thin sections (30 μm). Pictures **a** through **k** were taken with transmitted light only, whereas picture **l** was taken with concurrent reflected and transmitted light. **a** Sample 7:6-1; bubbles in clear glass. **b** Sample 7:4-5; glass with oxide and silicate microlites; few bubbles (*one indicated with an arrow*) but all round or ellipsoid. **c** Sample 7:3-7; lack of clarity in bulk of sample is due to xenolith powder, oxides and silicate microlites; darkest regions are pumiceous (*dark due lots of surfaces with contrasting refractive indices*). **d** Sample 7:3-10; banded sample; bubbles used for shape analysis are within the clearest band; opaque bands are pumiceous or contain xenoliths; grey band near bottom has relatively high silicate microlite content. **e** Sample 7:5-8; bubbles in clear glass. **f** Sample 7:3-3; clear glass with bubbles and low microlite content; dark bands at top and bottom contain xenolith powder; the *vertical grey area* at the *right* under the label 'f' is an artifact due to the surface of the sample being at an angle to the polished surface. **g** Sample 7:4-2; bubbles in clear glass; the two thin dark bands (nearly vertical) have high microlite contents; the *grey in the upper left* portion of the sample is due to the sample edge being at an angle to the polished surface. **h** Sample 7:4-3; bubbles in glass banded by microlite content; **i** sample 7:3-2; bubbles in clear glass with microlites; some bubbles are missing pieces; darker region has smaller bubbles with higher bubble number density. **j** Sample 7:5-7; bubbles in clear glass; at *top* is an area with less deformed bubbles and higher bubble number densities. **k** Sample 7:4-1; deformed bubbles in clear glass and planes of less deformed, irregular bubbles cutting the overall bubble texture. **l** Sample 7:2-9; macroscopic xenolith (rough, at *right*), clear glass with bubbles (*white*), glass with xenolith powder (smooth, *grey*)

shear stress calculations based on bubble shapes do not involve viscosity, and therefore provide more rigorous constraints on the deformation history of obsidian clasts.

Physical characteristics of samples

Grain size and componentry

Both grain size and componentry of our samples change with stratigraphic height (Fig. 2). Median grain size data from sieving bulk samples collected over 10 cm intervals show an overall trend of fining from the base to the distinct ash layer at the top of the Lower NP. Above this ash layer, there is an abrupt increase in grain size followed by a decrease in the upper half of the Upper NP (Fig. 2a). In detail, there are numerous smaller scale changes in grain size, including two ash layers near the top of the section at heights of 2.2 and 2.45 m.

Obsidian pyroclasts ≥1 mm comprise 1–6 wt.% of the NP bulk samples, whereas lithic clasts (defined here as dense clasts that are not obsidian) ≥6 mm comprise 2–26 wt.%. There is no correlation between median grain size and obsidian or lithic clast content in the Lower NP. However, variations in the obsidian content shadow changes in the lithic content (Fig. 2b): the relative proportions of both clast types decrease (from bulk samples 1 to 2 to 3), then increase (3 to 4), decrease (4 to 5) and increase (5 to 6). These variations are more pronounced if one examines the proportion of the juvenile component (rather than the entire deposit) that is obsidian. The pattern is broken immediately above the ash layer that marks the boundary between the Lower and Upper NP. Here the obsidian content reaches its maximum of 6 wt.% whereas the lithic content is at its minimum of 2 wt.%. In contrast to the Lower NP, there is no clear correlation between obsidian and lithic content in the Upper NP. However, with the exception of the base of the Upper NP, the obsidian content of the bulk samples increases with decreasing median grain size.

The relative proportions of different obsidian types also change with stratigraphic height (Fig. 2c), especially from the Lower to the Upper NP. Below the distinct ash layer that separates the two units, 95–97 wt.% of obsidian is either grey or black; immediately above the ash layer (bulk sample 7), only 30 wt.% of obsidian clasts are grey or black and the remaining 70 wt.% comprise obsidian mingled with pumice, bubbly obsidian, and clear obsidian with domains containing xenolith powder. Above the stratigraphic break, the proportion of these new clast types steadily diminishes as grey and black obsidian again dominate in both the upper part of the NP and in the Paulina Lake Ash Flow deposit.

Obsidian textures

The NP obsidian pyroclasts can be either homogeneous or highly heterogeneous, with bands or irregularly-shaped domains distinguished by abundance, size or shape of bubbles, crystals and xenoliths (Fig. 3). Boundaries between these texturally distinct domains are typically sharp. The glass is clear but has a greenish brown tinge if it is several hundred microns thick. The transparent glass of obsidian from the top of the Upper NP and the ash-flow deposit is slightly darker in color than glass lower in the NP. Additionally, throughout the pyroclastic deposits there are rare dark brown glass clasts that are compositionally indistinguishable from the clear glass, probably a consequence of submicroscopic oxide crystals (e.g. Schlinger et al. 1988).

Up to a third of the obsidian pyroclasts in a given bulk sample contain macroscopic xenoliths or opaque bands that contain microscopic xenolith powder. However, xenolith powder is also found in a subset of polished samples from all the textural categories listed in Fig. 2c, especially in clasts that appear black before polishing. All obsidian clasts with macroscopic xenoliths also have glassy regions containing xenolith powder (dominantly micron to submicron particles) (e.g. Fig. 4). For samples that are a few hundred microns thick, both the macroscopic xenoliths and the glass containing dispersed xenolith powder are opaque to transmitted light on a standard petrographic microscope.

Table 2 FTIR (H_2O and CO_2 contents) and bubble shape analysis (shear stress, shear rate, maximum dimensionless bubble elongation, bubble deformation time) results for samples shown in Fig. 3

Sample		H_2O (wt.%)	CO_2 (ppm)	σ (kPa)	Log $\dot{\gamma}$ s^{-1}	Max. *l*/*r*	Def. time (h)
A	7:6-1	1.25	5	0.8	−3.6	1.58	1.8
B	7:4-5	0.46	1	4.6	−4.0	1.89	5.3
C	7:3-7	0.72	10	79.1	−2.3	3.8	0.2
D	7:3-10	1.12	5	4.1	−3.0	3.24	1.0
E	7:5-8	1.34	2	1.9	−3.1	1.99	0.8
F	7:3-3	0.90	4	12.8	−2.8	1.8	0.3
		0.94	17				
		0.90	22				
G	7:4-2	1.05	3	0.4	−4.1	1.06	3.9
H	7:4-3	0.66	1	1.5	−4.2	1.62	7.9
I	7:3-2	1.03	4	3.5	−3.2	3.18	1.5
J	7:5-7	1.15	2	4.5	−3.0	5.3	1.3
K	7:4-1	0.87	4	3.9	−3.2	3.96	1.9
L	7:2-9	0.70	36	88.0	−2.3	2.9	0.2

The times in the final column are minimum bubble deformation times except for samples f and l. See text for details.

The xenoliths may be fragments of the same wall rocks that were erupted as discrete lithic clasts, however, we have not examined either in detail.

The prevalence of parallel bands with distinct textures in obsidian from lava flows and pyroclasts may result from fragmentation, annealing and shearing (Gonnermann and Manga 2003; Smith 1996; Tuffen et al. 2003). Such bands are common in the Newberry obsidian pyroclasts (e.g. Fig. 3c, d, f, h). More direct evidence of breaking and annealing of the Newberry obsidian pyroclasts includes (1) glass fragments with sharp boundaries within glass containing xenolith powder, and (2) planes of irregularly-shaped bubbles that appear to be partially healed fractures (e.g. Fig. 3k), which in some cases cross other textures (Rust et al. 2004). These observations, together with bubble deformation data and the distribution of H_2O and CO_2 within the clasts, help to constrain whether obsidian pyroclasts with breccia textures (clasts composed of fragments of glass) form (1) in a high shear environment near conduit walls, or (2) by welding and rheomorphism of pyroclasts and lithic clasts deposited in the vent region.

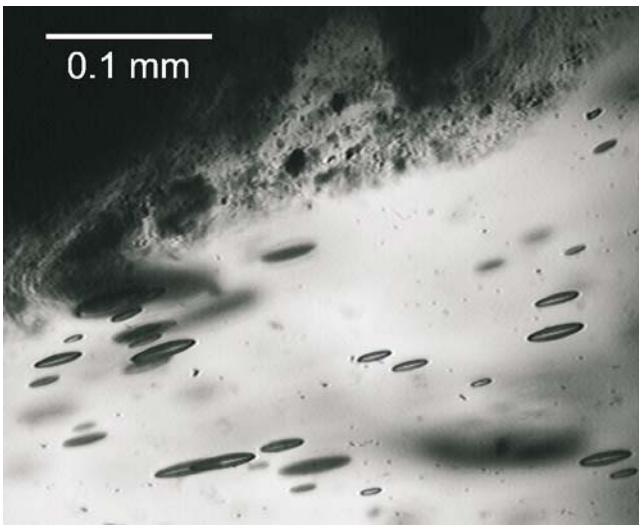

Fig. 4 Photomicrograph of sample **l** of Fig. 3 in transmitted light only, showing ellipsoid bubbles in clear glass (*lower right*) and glass with xenolith powder (*upper left*)

Symmetrical ellipsoid bubbles (+/− pointed ends) are common in Newberry obsidian pyroclasts; however, some clasts include bubbles that are highly irregular or largely collapsed (e.g. Fig. 5a). Other clasts have regions with anomalously high bubble number densities (e.g. Fig. 5b) similar to textures produced experimentally by delayed, homogeneous nucleation of rhyolite melt (Mangan and Sisson 2000). The strangest bubbles have regular boundaries but are missing parts (i.e. glass rather than gas; Fig. 5c, d). Here irregular but somewhat round bubbles appear to have once been part of a much larger bubble (Fig. 5d). As these textures are similar to those in planar arrays of irregular round bubbles in NP clasts, we suggest that these odd bubble shapes represent annealing of fractures that intersected the bubbles.

Volatile contents of obsidian clasts

FTIR data can be used to examine (1) differences between samples with and without xenoliths, (2) relationships between H_2O content and microtextures, (3) overall H_2O vs. CO_2 trends and implications for degassing mechanisms, and (4) changes in volatile contents of obsidian with time during the eruption.

Volatiles and xenoliths

Obsidian clasts that do not contain xenoliths have nearly uniform volatile contents. As a suite, these samples show a range in H_2O (0.1–1.5 wt.%), ≤6 ppm CO_2, and average CO_2 contents that increase slightly with increasing H_2O

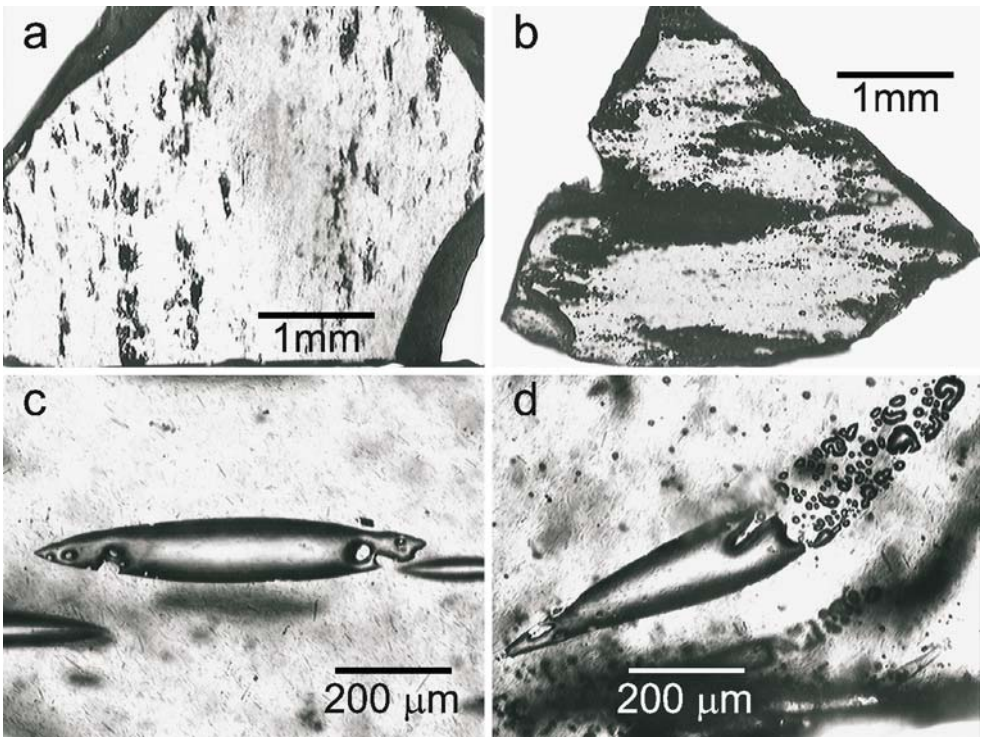

Fig. 5 Examples of irregular bubbles in obsidian pyroclasts from the Newberry Pumice. **a** Clusters of irregular bubbles (*dark*), possibly resulting from bubble collapse. **b** Clouds of bubbles (*dark regions*) in glass. **c** and **d** Bubbles with definite outlines but missing portions possibly due to healing of fractures in the melt that intersected the bubbles

(Fig. 6). In contrast, the CO_2 contents of glass in clasts containing xenolith fragments range from <1 to 66 ppm, mostly within a relatively narrow range in dissolved H_2O (0.5–1 wt.%). The amount of CO_2 dissolved in the glass decreases with distance from domains containing xenoliths (Figs. 7, 8), probably reflecting partial assimilation (decarbonation without melting) of carbonate-bearing xenolith fragments. Drilling in Newberry Caldera approximately 2 km north of the 1300 B.P. vent shows that hydrothermal calcite is common in the intracaldera volcanic and sedimentary facies, at least to the base of drilling at 932 m depth (Bargar and Keith 1999; Keith and Bargar 1988). In samples with CO_2 gradients, the water content usually increases with distance from the domains containing xenoliths. Exceptions include a sample (Fig. 8a, b) for which CO_2 content decreases with distance from two xenolith bands but H_2O increases with distance from one band, and decreases with distance from the other band (with a 1 mm-wide zone of bubbles in the glass adjacent to it). An extreme example of highly variable, non-systematic variations in both H_2O and CO_2 contents in a xenolith-glass breccia is shown in Fig. 8 (c and d), where CO_2 ranges from 3 to 36 ppm and H_2O from 0.57 to 0.82 over mm length scales.

H_2O content of xenolith-free clasts

Xenolith-free clasts have relatively low CO_2 contents, thus H_2O serves as a proxy for equilibration saturation pressure. In these clasts, bubble and crystal contents are crudely correlated with H_2O content of the glass (Fig. 9).

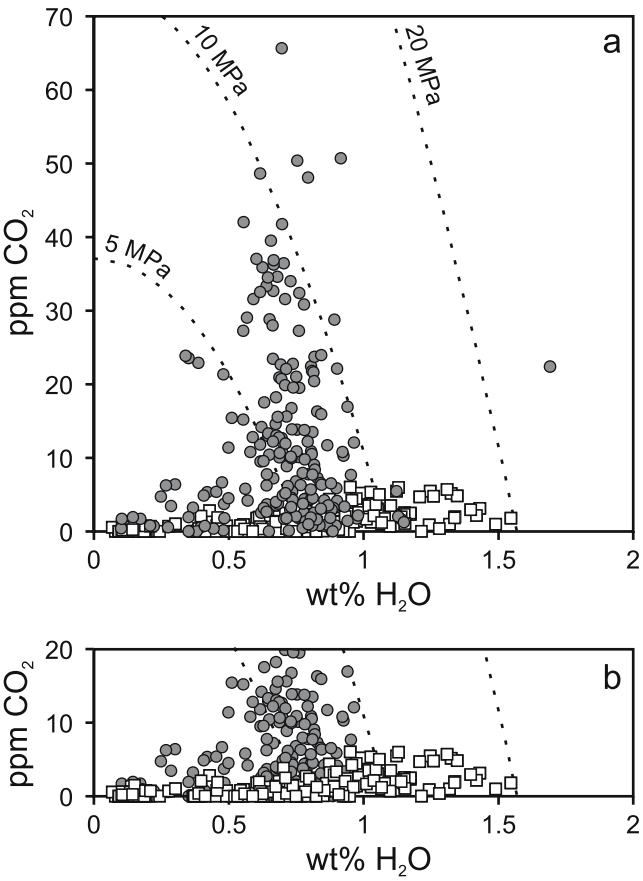

Fig. 6 CO_2 and H_2O contents of Newberry obsidian pyroclasts with xenolith powder (*grey circles*) and without xenoliths (*white squares*). Dotted lines are isobars. **a** Data for xenolith-bearing samples in forefront. **b** Data for for xenolith-free samples in the forefront

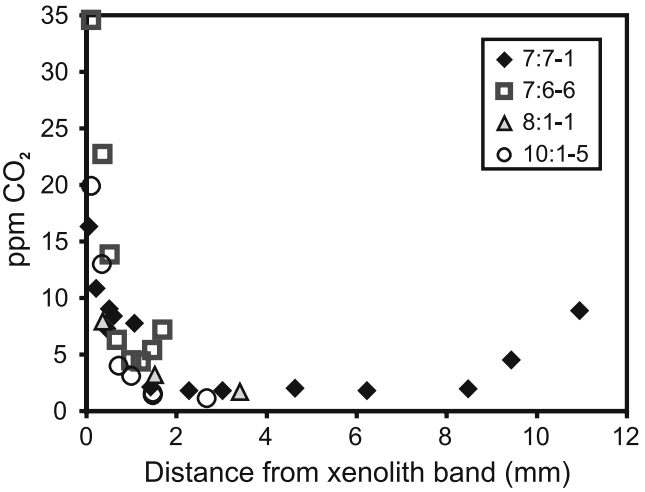

Fig. 7 CO_2 contents of glasses as a function of distance from xenolith bands in four samples. CO_2 content decreases with distance from xenolith-bearing bands but in samples 7:7-1 and 7:6-6, CO_2 begins to increase again as analyses approach additional xenolith bands. CO_2 data for sample 7:7-1 are shown on a picture of the clast in Fig. 8b. For this clast, distances are measured from the xenolith band at the base of the picture

In particular, obsidian clasts with numerous silicate microlites (c. 1 vol.%) have relatively low H_2O whereas those with either numerous distributed bubbles or mingled with white pumice tend to have relatively high H_2O contents. These trends indicate that H_2O exsolution was accompanied by both silicate microlite growth and bubble loss. However, clear obsidian clasts (those with few or no microlites or bubbles) exhibit the full range of H_2O contents measured: 0.1–1.5 wt.% for clear glass and 0.1–1.4 wt.% for dark brown glass. The development of different microtextures for the same H_2O content could be related to variations in cooling, decompression rate, stalling times or deformation histories of the magma (e.g. Castro and Mercer 2004). For example, microlite-rich glass may record shallow stalling and degassing of magma for several hours prior to eruption whereas clear obsidian with the same H_2O content may have degassed during ascent without stalling prior to rapid quenching either during eruption or by contact with cooler rocks. Variations in bubble content for clasts with similar glass H_2O content could record heterogeneous patterns of bubble nucleation on a scale larger than the obsidian pyroclasts (Hammer et al. 1999; Wright et al. 2007) or differences in post-vesiculation gas loss.

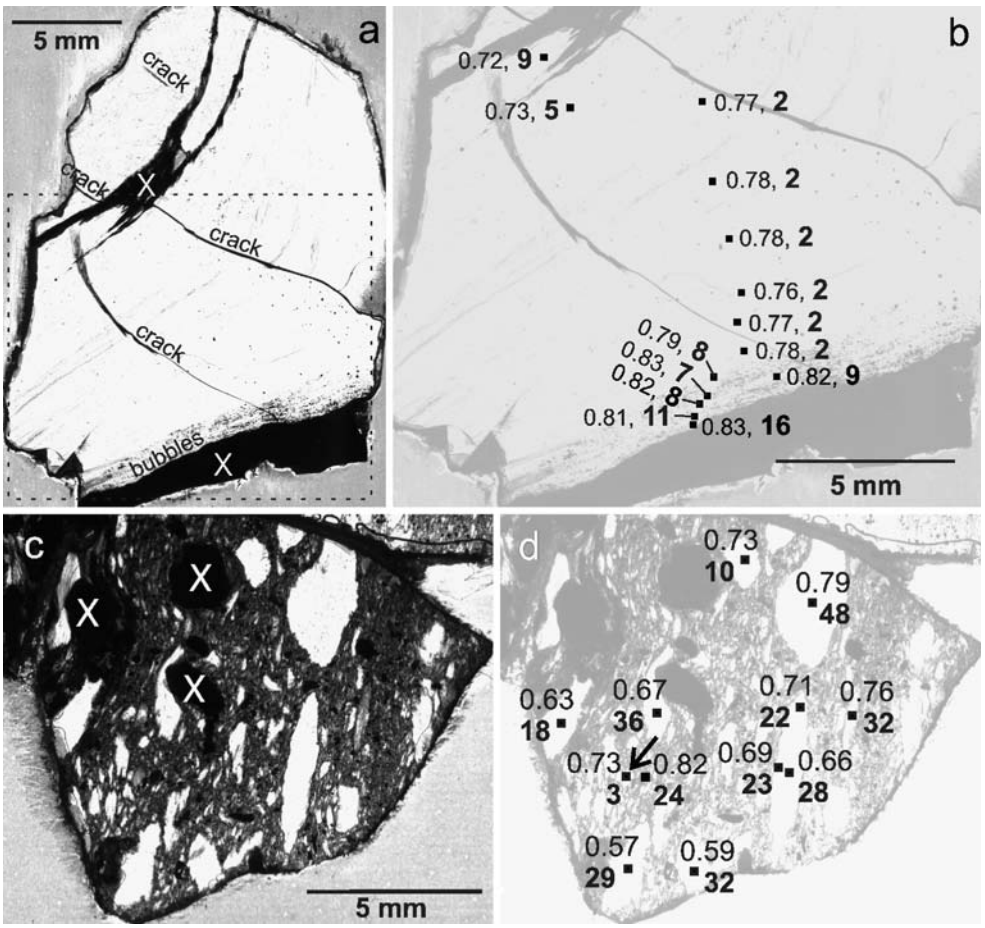

Fig. 8 Spatial variation in volatile contents in two large obsidian clasts from bulk sample 7. Picture **b** is an enlargement of the outlined region in **a**; **c** and **d** are identical pictures (except for brightness and contrast) of a second clast. *Numbers in bold* (>1) are ppm CO_2, and *adjacent numbers* (<1) are wt.% H_2O. In **a**, *X* indicates glass with xenolith powder; in **c**, *X* mark the three largest xenoliths. The *arrow* in **d** points to an area where further analyses were done that are discussed in the text related to CO_2 diffusion time scales

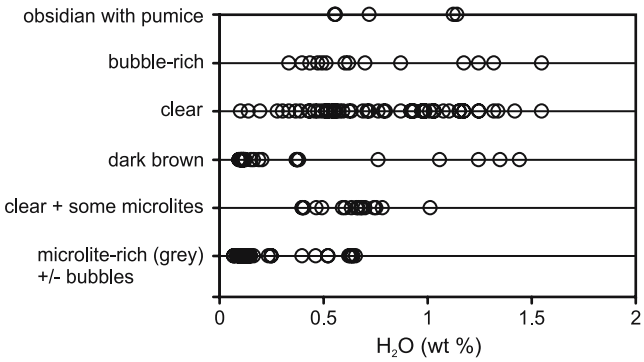

Fig. 9 H_2O contents of obsidians from bulk samples 1,3,6 and 7 sorted by textures: dense glass intercalated with pumice (*regions that are dominantly bubbles and appear white to naked eye*); clear glass with relatively high bubble content but thick bubble walls; clear glass with very few or no microlites; dark brown glass; clear glass with intermediate microlite content; clasts that appear grey due to relatively high microlite contents

H_2O–CO_2 trends

Only samples without xenoliths have been used to explore H_2O–CO_2 trends related to magma degassing. All clasts without xenoliths have ≤ 6 ppm CO_2 dissolved in the glass and show a slight decrease in CO_2 content with decreasing H_2O (Fig. 6). Many of the samples, including those with numerous microlites, have negligible CO_2 contents suggestive of open-system degassing. However, the CO_2 contents of many other NP samples are large enough to eliminate equilibrium open-system degassing as an explanation for the entire NP H_2O–CO_2 data set. The volatile data could also be explained by closed-system exsolution from melt with, for example, 4 wt.% dissolved H_2O, 600 ppm dissolved CO_2 and ≤1 wt.% initial exsolved vapor (Newman and Lowenstern 2002). However, as discussed above, the low vesicularity of obsidian requires that some form of open-system degassing (gas escape) occurred by late in the degassing history of each sample. One explanation for the observed volatile trend is open-system degassing buffered by vapors fluxing through the magma, as suggested by Rust et al. (2004) for obsidian from Mono Craters. Another possibility is disequilibrium open-system degassing where the slow diffusion of CO_2 relative to H_2O maintains high CO_2 / H_2O ratios in the melt (Gonnermann and Manga 2005).

Temporal changes in volatile contents

With only two exceptions, H_2O content of obsidian clasts remains below 1.5 wt.% (~20 MPa) throughout the stratigraphic sequence. However, the xenolith-absent clasts show both larger H_2O ranges and more stratigraphic variation than xenolith-bearing clasts. In particular, xenolith-absent clasts show a distinct increase in maximum water contents from the Lower NP to the Upper NP. This increase occurs as both an increase in the modal H_2O content for the distribution of measurements in any given bulk sample and in the absence of clasts with both low microlite and low water contents in most of the Upper NP (bulk samples 8 through 11), despite their presence in the Lower NP and near the top of the fall deposit (sample 12). Microlite-bearing H_2O-poor clasts, however, are inferred to be present throughout the sequence (as recognized by their grey color; Fig. 2).

The most striking stratigraphic variation in volatile content is the observed abrupt increase in CO_2 contents of obsidian pyroclasts containing xenoliths. In the Lower NP, CO_2 contents in these clasts are ≤6 ppm except for two clasts (4 analyses) with 14–42 ppm CO_2 (Fig. 10) from bulk sample 6, which is just below the ash layer that separates the Upper and Lower NP. CO_2 is most abundant in the bottom 20 cm of the Upper NP (bulk samples 7 and 8); the maximum CO_2 value in a given bulk sample then decreases upward. As CO_2 appears to have diffused into the melt from xenoliths, CO_2 enrichment provides evidence of stalling of magma at shallow depths such that there is time for CO_2 diffusion. It is possible that the two CO_2-rich clasts in bulk sample 6 are from higher in the stratigraphic section and were accidentally included during sample collection. However, the higher H_2O contents of all the xenolith-bearing clasts in bulk sample 6, as well as the higher proportion of relatively H_2O-rich clasts compared to lower in the stratigraphic section, suggest that there was a real change in the volatile contents of obsidian pyroclasts just before the ash layer was deposited.

There is an up-sequence increase in CO_2 contents of xenolith-free clasts beginning immediately below the Lower–Upper NP boundary. Increasing CO_2 could result from either an increase in gas flux through the magma (Rust et al. 2004) or from degassing conditions becoming farther from equilibrium (Gonnermann and Manga 2005) at the boundary. We believe the former to be more likely, as variations in grain size, proportions of clast types and obsidian textures (Fig. 2) all indicate an abrupt change in eruption dynamics at the Lower–Upper NP boundary that can be explained by a temporary pause in eruptive activity. Such a pause would permit time for volatile contents to be closer to rather than further from equilibrium. Furthermore, the pause provides time for both permeable flow of gases through the conduit plug (potentially increasing CO_2 levels) and re-pressurization of the system.

Bubble geometry (flow parameter) analysis

To better characterize physical processes that contributed to the Lower–Upper NP transition, we measured the dimen-

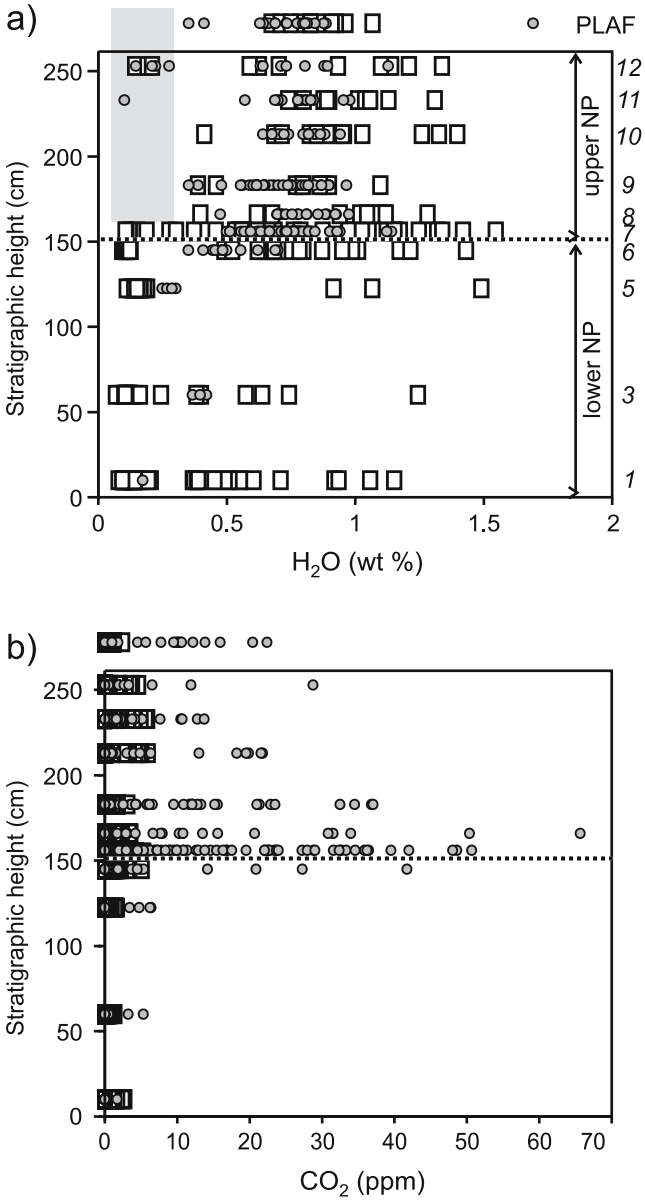

Fig. 10 Variations in H_2O (**a**) and CO_2 (**b**) as a function of stratigraphic position in obsidian pyroclasts from the Newberry Pumice (NP) and Paulina Lake Ash Flow (PLAF). *Grey circles* are clasts that contain xenoliths and *white squares* are xenolith-free clasts. The *dotted line* shows the location of the ash that is the boundary between the lower and upper Newberry Pumice. **a** Numbers at right are bulk sample numbers. The *shaded region* highlights the lack of low H_2O samples measured above bulk sample 7, which is in large part due to not analyzing grey obsidian (see text for details)

sions of bubbles from 12 clasts from the base of the Upper NP (Fig. 3). These clasts contain bubbles with a wide range in sizes and aspect ratios (Fig. 11). In a given sample, there is an overall trend of greater bubble deformation with increasing bubble size because surface tension stresses are less for larger bubbles. However, if the shear stress for two samples differs, then bubbles of the same size in the two samples will have different aspect ratios. Relatively low stresses are recognized by large (and small) bubbles being fairly round, whereas relatively high stresses will deform even the small bubbles. For example, in Fig. 11 we see a large and barely deformed bubble in one sample (low shear stress), and much smaller but highly deformed bubbles in another sample (higher shear stress).

Linear fits to the *D*–*r* data (Figs. 11, 12a), allow each bubble size (*r*) to be converted to a capillary number *Ca*. Plotting the bubble deformation parameter *D* versus the dimensionless *Ca* should collapse the twelve data sets to a single curve if the only difference in the flow regime for the samples is the magnitude of the stress driving flow. Although data from most samples do follow a single curve, the data from two samples diverge dramatically from the other Newberry samples as well as from the results of simple shear experiments (Rust and Manga 2002) (Fig. 12b). $D=1$ is the theoretical high deformation limit for both simple and pure shear. In samples f and l (Fig. 3), however, *D* approaches a much smaller value (0.4 and 0.65, respectively). These data are not explained by a drop in stress and consequent rounding of bubbles by surface tension (Rust and Manga 2002; Rust et al. 2003). Instead, the simplest explanation is that bubble deformation is limited by the amount of accumulated strain, such that if steady shearing had continued for longer then the larger bubbles would have been more deformed. The finite strain preserved in samples f and l allows us to calculate strains and corresponding deformation times (in addition to shear rates and stresses) for these clasts.

Assessing shear rates (stress/viscosity) from bubble deformation is complicated by the sensitivity of melt viscosity to H_2O content, particularly over the range of H_2O contents of these samples (e.g. Hess and Dingwell 1996). For this reason we use measured glass H_2O together

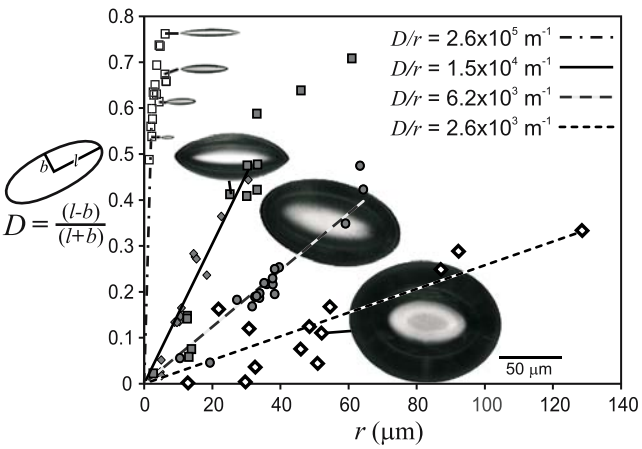

Fig. 11 Subset of bubble deformation data showing linear *D*(*r*) fits, where *D* is a dimensionless measure of bubble deformation and *r* is the radius of a sphere of the same volume as the bubble. See Fig. 3 and Table 2 for symbol legend. *Short lines* join bubble pictures to their corresponding data point. All pictures are at the same scale

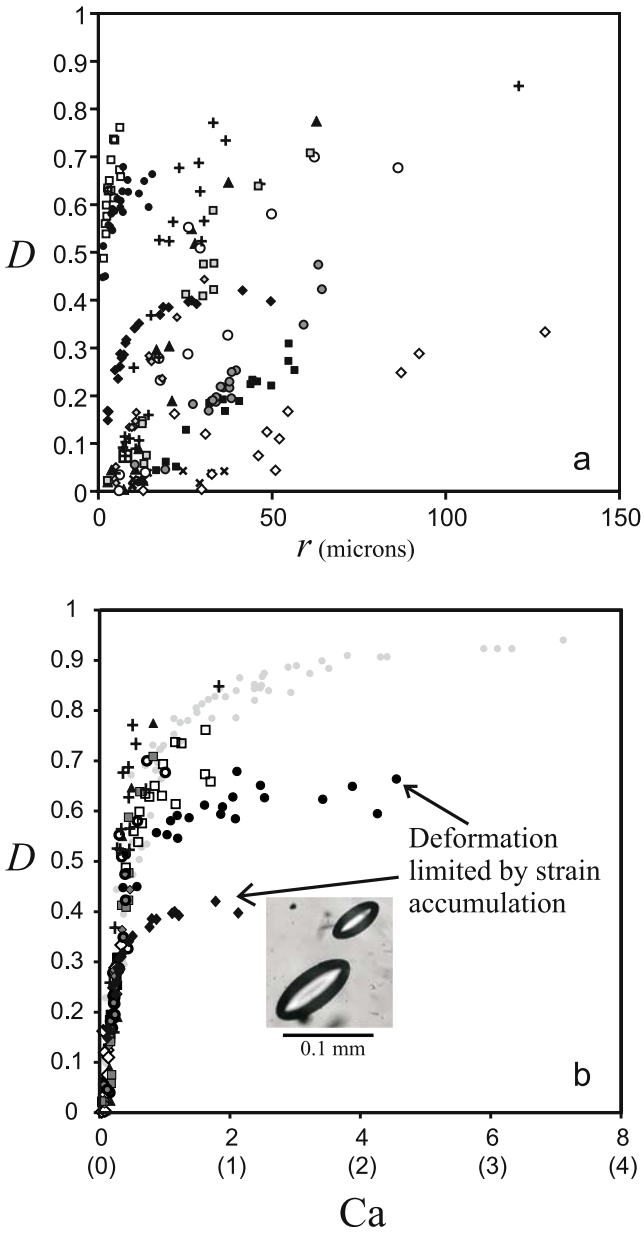

Fig. 12 **a** Bubble deformation parameter D vs. bubble radius for bubbles in the twelve samples shown in Fig. 3. **b** Bubble deformation parameter D vs. capillary number (Ca) for the same samples and experimental data (*pale grey circles*) from Rust and Manga (2002). Capillary numbers calculated from bubble shapes assuming simple shear are directly below the axis of abscissas; capillary numbers calculated assuming pure shear are indicated with brackets. The bubble deformation in two samples corresponding to Fig. 3f (*filled diamond*) and 1 (*filled circle*) seems to be strain-limited because in each case, as Ca is increased, D approaches a limit much less than 1. Inset shows adjacent bubbles in the clast shown in Fig. 3f with similar shapes but different sizes

with bubble deformation data to assess shear rates from Ca/r values (Fig. 13; Table 2). Here we assume simple shear flow, a surface tension of 0.3 N/m, and a melt temperature of 850°C. The resulting shear stresses and shear rates vary by more than two orders of magnitude. Data from most samples lie between 1–10 kPa and 10^{-4}–10^{-3} s^{-1}, respectively. The maximum measured shear stress is 88 kPa and the maximum shear rate is $10^{-2.3}$ s^{-1}, similar to estimates from a South Sister volcano obsidian pyroclast analyzed by Rust et al. (2003).

In addition to shear rates and stresses, bubble geometries provide information on deformation style (pure or simple shear), which is useful for understanding physical mechanisms of obsidian formation. In pure shear, bubbles are oriented parallel to the flow direction, but in simple shear the angle between the longest axis of a bubble and the flow direction (θ) varies with Ca. For bubble orientation analysis, it is ideal to have the sample oriented on the microscope with both the flow direction and velocity gradient parallel to the stage, as other orientations reduce the apparent value of θ. However, in selecting samples for bubble analysis from those prepared for FTIR, we required only that the flow direction be approximately parallel to the polished surface, noting that non-ideal orientations of samples reduce the apparent simple shear component. Another problem is that the flow direction is not always evident, as illustrated by sample f, where the flow direction is not clearly indicated by microlite orientations, perhaps because of the limited amount of strain (Table 2). In this sample the bubbles are at a large angle to bands defined by xenolith powder. If flow were parallel to the bands this orientation would suggest simple shear, however the bands are not necessarily indicative of flow direction.

Despite some ambiguity in deformation analysis, we find clear evidence for both pure and simple shear in samples

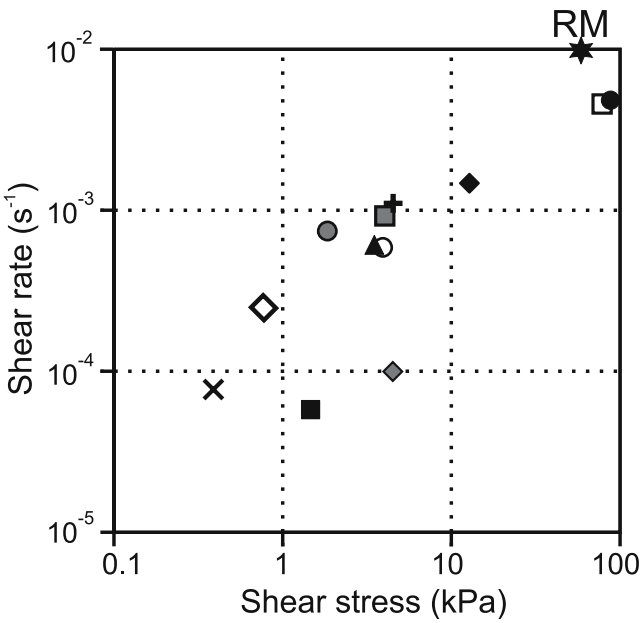

Fig. 13 Shear rates and stresses determined from bubble shape analysis for the twelve samples in Fig. 3 (also listed in Table 2) and the obsidian pyroclast from Rock Mesa (RM) examined in Rust et al. (2003)

that are well oriented for this analysis. For example, bubble orientations in sample h of Fig. 3 indicate a strong component of simple shear because bubble elongation is oriented at an angle to the flow direction and θ tends to be smaller for more deformed bubbles. In contrast, bubbles in sample d of Fig. 3, which is also well oriented for θ measurement, indicate dominantly pure shear. Finally, bubble textures in some clasts preserve evidence of complicated flow regimes. Within clast l, for instance, there are variations in both flow direction and bubble deformation that provide evidence for large changes in shear stress even at mm scales. This variation is not evident in the bubble geometry data presented here because we limited our analysis to a small region and thus examined local flow parameters.

Origins of breccia textures

The textures of many NP obsidian pyroclasts record a history of breaking and annealing that could reflect either shearing near conduit walls as magma ascends or welding and refragmentation of fallback. High shear stresses near conduit margins may cause magma to break and anneal (possibly multiple times) during ascent (e.g., Gonnermann and Manga 2003). The high shear stresses that fracture silicate melt could damage and pulverize the adjacent wall rocks, providing a source of xenolith powder observed in many obsidian clasts, including almost all clasts with breccia textures. Several observations are consistent with this model for the NP obsidian: (1) the presence of clasts composed of angular glass fragments within a glassy matrix (commonly including xenolith powder), (2) the presence of partially healed fractures in glass, (3) the incorporation of xenoliths, (4) bubble analysis showing that samples with the highest shear stresses and shear rates also contain xenoliths, and (5) the overall trend of the CO_2/H_2O data (Rust et al. 2004). The autobrecciated clast type may be more common in pyroclastic deposits produced after ascent of magma to shallow levels (base of Upper NP) because autobrecciation and incorporation of xenoliths are likely to accompany excavation of new pathways through the wall rock during the pause.

Some NP obsidian pyroclasts (e.g., Fig. 8c and d) have textures and volatile contents that require that fragments with very different volatile contents annealed and quenched faster than volatile re-equilibration. Shearing along conduit walls could bring together fragments from a range of pressures and depths and thus volatile contents (e.g., volatile data in Fig. 8d correspond to equilibration pressures of 4.5–11.8 MPa for 850°C). Transport in tuffisite veins could also rapidly bring together clasts from different sources. However, veins such as those described by Tuffen et al. (2003) and Stasiuk et al. (1996) do not have sufficient vertical extent to explain the range of volatile contents in some NP clasts. An alternative explanation is welding of hot fallback with the weight of accumulated clasts driving deformation and porosity reduction. The stresses required to produce the observed bubble deformations in analyzed obsidian clasts from the base of the Upper NP are equivalent to pressures generated by 4 m of bubble-free overlying magma, or ≥20 m of unconsolidated pumice.

Accumulation, compaction and welding of meters of fallback within the vent funnel are most likely during eruptive pauses. Several obsidian pyroclasts from the base of the Upper NP, which we infer to follow a pause, show textures consistent with this origin (e.g., flattened but not substantially sheared fragments in Fig. 8c and d). However, accumulation and welding in the vent does not seem viable during the sustained, erosive and explosive activity that characterized most of the NP, which continuously erupted ~10 wt.% lithic clasts. Pyroclasts could weld on the ground adjacent to the vent during continuous explosive activity and be re-fragmented as the vent widens or migrates, perhaps also explaining the trace component of pumice aggregate that appears throughout the Newberry Pumice (Kuehn 2002). However, we would expect the resulting fall deposit to contain a more substantial lithic portion (e.g. possibly bulk sample 11).

We conclude that the appearance of abundant brecciated clasts at and above the ash layer that defines the Lower–Upper NP boundary is consistent with physical mechanisms inferred to operate during a pause. Specifically, we expect that the slow approach of magma to shallow levels between explosive episodes would allow sufficient time for degassing, brecciation and annealing of fragments. We suggest that most of the brecciated and/or banded obsidian pyroclasts formed by autobrecciation but that others formed by welding of fallback clasts that were re-fragmented and re-incorporated into the eruption column.

Time scales

Bubble shape and volatile concentration data provide constraints on time scales of volcanic processes that can be applied to questions of conduit flow and welding. In particular, strain determined from maximum bubble elongation divided by strain rate calculated from bubble shapes as a function of size gives the flow time to deform bubbles. Furthermore, length scales of CO_2 diffusion in xenolith-bearing clasts, together with CO_2 diffusivity based on experimental data, provide estimates of the contact time between hot melt and xenoliths. Similarly, length scales of H_2O and CO_2 variations in welded breccia constrain the contact time of hot clasts within the breccia. Both

diffusional and bubble deformation time scales can also be compared with viscous welding time scales calculated from viscosity and maximum load estimates. Together, these estimates allow us to bracket different eruptive time scales.

Time scales for bubble deformation are calculated for the two clasts (f and l) where the deformation of the largest bubbles is strain-limited (Fig. 12b); for other clasts we calculate minimum deformation times. We approximate strain using the maximum dimensionless elongation of the bubble (l/r, where l is the semi-major axis of the most deformed bubble, and r is the radius of the undeformed bubble). Dividing the strain by the shear rate calculated from the shapes of the least-deformed bubbles gives flow times of about 20 and 10 min for samples f and l, respectively (Table 2). Similarly, taking the maximum l/r in other clasts to indicate minimum strain, we calculate minimum deformation times for the other samples to range from 10 min (clast c) to almost 8 h (clast h). These calculations assume 850°C; for a lower/higher temperature, the calculated deformation time is longer/shorter due to the dependence of melt viscosity on temperature. The two longest minimum deformation times (5 and 8 h) correspond to the two crystal-rich (grey) clasts. A timescale of hours is consistent with both experimental and observational data on decompression-driven crystal growth in silicic melts (e.g. Hammer et al. 1999; Hammer and Rutherford 2002). Of these two samples, one has bubble orientations that indicate dominantly simple shear whereas the deformation regime responsible for the other clast is inconclusive. In contrast, the three shortest deformation times (10–20 min) correspond to three of the four clasts that contain xenoliths and are the three clasts with the highest CO_2 contents. The fourth xenolith-bearing clast also has relatively short deformation time (1 h). As discussed earlier, there is evidence for both pure and simple shear in xenolith-bearing clasts and the flow regimes can be complex. For example, the bubbles in the xenolith-bearing clast l (Fig. 3) indicate variations in both flow direction and stress at scales as short as millimeters.

We attempt to estimate the contact time of xenolith powder with hot melt using CO_2 diffusion profiles away from bands of xenolith powder (Figs. 7, 8b). Due to large uncertainties in the required input parameters (experimental CO_2 diffusivity data, temperature, geometry of source, CO_2 concentration of source), we do not calculate model diffusion profiles but instead calculate a time scale for diffusion by dividing the squared characteristic length scale by CO_2 diffusivity. CO_2 diffusion profiles (Fig. 7) suggest a length scale of order 0.5 mm. For the water contents of the glasses (0.7–1 wt.%) and a temperature of 850°C, the diffusivity of CO_2 is about 10^{-13} m^2/s (Behrens and Zhang 2001; Watson 1991). This calculation gives a diffusion time of about a month, which would imply incorporation of xenolith powder into the melt long before clast quenching. However, the same clasts have very low microlite contents that seems inconsistent with this time scale, perhaps a consequence of poor controls on the temperature and CO_2 diffusivity used for this calculation. Also, non-ideal orientations of polished surfaces with respect to CO_2 sources would cause overestimates of diffusion time. Another diffusion time scale is provided by the clast shown in Fig. 8c, d. We inferred that this clast formed by welding in or near the vent, as discussed above. FTIR data for this sample indicate that there was insufficient time for CO_2 to equilibrate prior to quenching, as analyses <0.2 mm apart (within the clast labeled with an arrow in Fig. 8d) differ in CO_2 content by more than four fold with no detectable difference in water content. This limiting distance allows us to calculate a CO_2 diffusion time of less than 5 days, given the same conditions used above. We can further bracket times using the lack of H_2O variation between the same two points if we assume that the clasts started with different H_2O values. H_2O homogenization over 0.2 mm would require at least 11 h, assuming a diffusivity of 10^{-12} m^2/s (Zhang and Behrens 2000). These time scales are longer than those obtained from bubble deformation analysis.

Finally, we can calculate a time scale for welding (annealing) by viscous flow by dividing the melt viscosity by the applied load (Sparks et al. 1999). If we take the load to be the range of stresses calculated from bubble shapes, the viscous welding time scale is the reciprocal of the shear rates (Table 2). These timescales vary from about 3 min to 4 h, similar to the estimated bubble deformation time scales. Moreover, as for the bubble deformation analysis, the shortest times correspond to xenolith-bearing clasts, although it should be noted that the welding and bubble deformation time calculations are not independent. Additionally, all of these time scales depend on the assumed melt temperature; for example, the disparity between the time scales for xenolith-bearing and microlite-bearing clasts would be eliminated if the melt containing xenoliths was about 100°C cooler than the microlite-bearing melt.

In summary, although there are uncertainties in input parameters that limit the utility of calculated time scales, both bubble deformation analysis and estimates of viscous annealing indicate flow for minutes to hours. For both bubble deformation and annealing, estimated time scales are shortest for xenolith-bearing clasts and longest for microlite-rich clasts. Time scales of hours for microlite-bearing clasts are also consistent with crystallization time scales anticipated for near-surface conditions (e.g. Couch et al. 2003; Hammer and Rutherford 2002). Finally, although time scale differences controlled by temperature variations are possible, they do not explain the variations in shear stresses determined from bubble shapes, which are greatest for the xenolith-bearing clasts and least for the microlite-rich clasts.

Origins of obsidian pyroclasts and evolution of the 1300 B.P. Newberry eruption

The generation of obsidian pyroclasts requires fragmentation of low vesicularity melt or glass and incorporation of these fragments into an eruption column or density current. There are numerous potential sources of obsidian in the NP: (1) preexisting obsidian domes, glassy welded tuffs or dikes from prior eruptions, (2) vanguard magma, (3) syneruptive degassing in the conduit, and (4) syneruptive welded fallback. Indeed, H_2O–CO_2 contents and textures of obsidian, as well as the proportions of lithic clasts and obsidian in bulk samples, suggest that there were multiple origins of obsidian, and that the dominant source changed during the eruption.

H_2O–CO_2 contents of glasses provide constraints on the pressure and source depths of obsidian pyroclasts. With one exception, H_2O–CO_2 contents of the NP obsidian correspond to equilibrium saturation pressures <20 MPa, mostly between 3 and 10 MPa (Fig. 6). 20 MPa is equivalent to about 900 m depth in magma with a density of 2300 kg/m^3, indicating that most of the NP samples come from relatively shallow depths. Importantly, however, the volatile content of most of the obsidian clasts is sufficiently high to preclude prior obsidian domes as a source. Theoretical models (e.g. Dobran 2001), drill holes (Eichelberger 1989) and dissections through older conduits (e.g. Stasiuk et al. 1996), indicate that erosion during explosive eruptions causes vent regions to flair, suggesting that the NP vent funnel could have extended to depths of hundreds of meters. Thus, much of the magma that became obsidian pyroclasts was probably at pressures equivalent to lithostatic loads for the depth range of the vent funnel.

Based on componentry and the total volume of the NP, ~10^{-2} km^3 of wall rock were ejected during the NP eruption, primarily as discrete lithic clasts with only 10^{-5}–10^{-6} km^3 as xenoliths in obsidian pyroclasts. There was no pre-existing conduit and the volume of wall rock erupted probably reflects the volume of the conduit excavated by the eruption, which for a cylindrical conduit with a radius 50 m, gives a depth of ~1.3 km. It is likely that magmatic volatiles released in advance of the rising magma, as well as heating of ground water, altered and fractured the shallow country rocks, thus helping the propagation of a pipe-like conduit. Such pre-eruption fragmentation would also aid in the incorporation of xenoliths in the magma. Xenoliths are common in the obsidian pyroclasts but based on a very limited study, they are uncommon in pumice. This pattern suggests that obsidian tends to form near contacts with wall rocks.

The relative proportions of obsidian and lithic clasts provide further constraints on obsidian origin. Bulk samples of the Lower NP show that the abundance of obsidian and lithic clasts follows similar patterns despite differences in overall abundance (Fig. 2). Moreover, these variations do not appear to correlate with changes in median grain size (a measure of eruption intensity). This shadowing of obsidian and lithic contents is most easily explained if both obsidian and the wall rock source of the lithic clasts were excavated together as the conduit widened. From this perspective, the pattern is most easily explained if the obsidian was in dikes in the wall rocks rather than lining the wall of the existing conduit. For example, the relatively constant lithic: obsidian ratio could result from erosion of a cylindrical conduit through a dike that initially brought magma to shallow levels, or the erosion of magma-filled fractures that are offshoots of the conduit. This interpretation is also consistent with the limited range of obsidian types preserved within the Lower NP.

The median pumice size decreases upward through the Lower NP (Fig. 2), suggesting a stable eruption that diminished in intensity through the first part of the subplinian phase. Throughout this part, there are no significant changes in the range of either H_2O or CO_2 contents of the glasses except immediately below the distinct ash layer at the top of the Lower NP (Fig. 10). Furthermore, the only textural change is a decrease in the relative proportion of grey (microlite-bearing) to black obsidian clasts. The high percentage of grey obsidian clasts at the NP base suggests that the earliest stage of magma ascent was sufficiently slow to allow microlite growth during ascent. Slow initial magma ascent is also consistent with Kuehn's (2002) suggestion of minor pre-climactic explosive activity. On the basis of evidence from both obsidian and pumice clast size, we suggest that the obsidian of the Lower NP was derived, in large part, from precursory dikes and/or glass-filled fractures that represent early stages of conduit formation. A damage zone of broken rock and intercalated rhyolite has been observed at the margin of feeder dikes drilled at Inyo Dome (e.g. Carrigan and Eichelberger 1990; Eichelberger 1989; Heiken et al. 1988) and may be a common feature of silicic conduit development.

The style of the eruption changed at the Lower–Upper NP boundary, where obsidian content is greatest and lithic content is least (Fig. 2). Importantly, the basal Upper NP is the only part of the stratigraphic section where there is more obsidian than lithic clasts. A high proportion of obsidian to lithic clasts could be explained by disruption of a magma plug formed within the conduit between the eruption of the Lower and Upper NP. Additional evidence for plug disruption is the wide and evenly distributed range of volatile contents of this basal obsidian (Fig. 10), which is consistent with rapid downward propagation of a fragmentation front through variably degassed magma (e.g. Cashman and McConnell 2005). That the break in explosive activity was short-lived is suggested by the small proportion of microlite-rich grey

obsidian (e.g. Hammer et al. 1999), especially in comparison with obsidian erupted at the base of the Lower NP, and the short bubble deformation time scales. Finally, the maximum CO_2 contents of obsidian containing xenoliths are also greatest at the base of the Upper NP, indicating that the pause was long enough to allow decarbonation of fine xenoliths and CO_2 diffusion into the melt.

The basal Upper NP (bulk sample 7) also records the introduction of substantial fractions of obsidian with textures rarely found in the Lower NP: uniformly clear obsidian, obsidian mingled with pumice, bubbly obsidian, and clear obsidian with xenoliths or bands containing xenolith powder (Fig. 2c). These clasts probably have several different origins, including (1) welded fallback, (2) degassed magma in the plug, and (3) autobrecciated zones of the plug. These clasts have moderate to high water contents compared to the total range of H_2O in NP obsidian and each textural type has a characteristic H_2O range: clear obsidian has 0.3–1.5 wt.% H_2O, clear obsidian with bands of xenolith fragments has 0.4–0.9 wt.% H_2O, obsidian mingled with white pumice has 0.5–1.1 wt.% H_2O, and bubbly obsidian has 0.6–1.5 wt.% H_2O. The maximum equilibration pressures indicated by the volatile contents of clear and bubbly obsidian clasts (~20 MPa) may record the maximum thickness of the degassed, low vesicularity plug that overlay vesicular magma in the upper conduit just prior to the Upper NP eruption. Alternatively, the maximum water content may have been controlled by the relative rates of bubble nucleation and clast quenching, such that deeper, water-rich magma was able to nucleate and grow bubbles during rapid syn-eruptive decompression (e.g. Hoblitt and Harmon 1993; Wright et al. 2005). Both scenarios are consistent with the bubbly obsidian and obsidian mingled with pumice having relatively high H_2O contents, although only the former explanation provides an estimate of plug thickness.

After the initial fragmentation of the plug, the eruption returned to pre-pause conditions. The volumetric abundance of lithic clasts again exceeded that of obsidian and the abundance of obsidian mingled with pumice and clear obsidian (+/− xenolith bands and bubbles) gradually decreased until the obsidian componentry resembled that of the Lower NP. CO_2 levels of xenolith-bearing clasts also decreased to Lower NP values, suggesting that only the slow ascent and pause in explosivity during plug formation provided sufficient time for substantial CO_2 diffusion into the melt. Taken together, these data indicate that once the plug cleared, remnants of it continued to be excavated but in reducing quantity with time. The only puzzling part of this interpretation is the gradual decrease in CO_2 content of xenolith-bearing clasts. Perhaps these clasts are remnants of the cool outer margins of the plug, or perhaps lateral excavation of the vent was sufficiently slow to permit some amount of CO_2 diffusion within small dikes prior to eruption.

Additional evidence for continued vent widening during the Upper NP lies in the presence of several ash layers in the Upper NP, as well as variations in the clast sizes in intervals between the ash layers (Kuehn 2002). We interpret these ash layers to be deposits of density currents shed from the eruption column that, despite instabilities, maintained a vigorous column (e.g. Gardner et al. 1998; Wilson and Hildreth 1997). Both incipient instability of the eruption column and decreasing column height during this time period are consistent with vent erosion. Moreover, the abrupt increase in lithic clasts toward the top of the Upper NP section suggests that vent widening may ultimately have caused full collapse of the column, deposition of the small-volume Paulina Lake Ash Flow, and subsequent effusion of the Big Obsidian lava flow, during which time magma ascent through the enlarged vent was sufficiently slow to permit extensive volatile loss by open-system degassing (e.g., Jaupart and Allegre 1991).

Comparison with the 650 B.P. Mono Craters eruptions

Obsidian pyroclasts from deposits of the 650 B.P. Mono Craters eruption sequence have also been examined in detail (Bursik 1993; Newman et al. 1988; Rust 2003; Rust et al. 2004; Sieh and Bursik 1986). In both the 1300 B.P. Newberry and 650 B.P. Mono Craters eruptions, the magma was rhyolite with very low crystal contents and the eruption sequence evolved from eruption columns, to pyroclastic density currents, to obsidian lava effusion. However, the Mono Craters eruption was episodic and involved multiple vents linked by a dike that eventually produced eight fall units and five lava flows or domes (e.g. Sieh and Bursik 1986), whereas the Newberry eruption produced a single fall deposit and a single lava flow from a single vent (Kuehn 2002). Pyroclasts from both eruptions are dominantly white pumice with lesser amounts of grey pumice and fresh dense obsidian. However, obsidian pyroclasts are limited to only a few percent of the NP deposit, whereas obsidian comprises up to 80% of the lower portion of one Mono Craters fall unit (unit 7, Sieh and Bursik 1986). Qualitative descriptions suggest there is also substantially more tube pumice in the Mono Craters deposits (Herd 1994; Sieh and Bursik 1986). We suspect that higher abundances of both obsidian and tube pumice at Mono Craters reflect the high surface area to volume ratio provided by the shallow feeder dike for this system. Here we explore this interpretation by examining pyroclastic obsidian produced by the two different feeder geometries.

Obsidian clasts from both eruptions contain xenolith powder as well as textures indicative of magma brecciation.

In addition, the highest proportion of microlite-rich obsidian is found at the beginning of both eruption sequences (Figs. 2, 14a), as might be expected for slow initial magma ascent toward the Earth's surface. However, there are also differences in obsidian clast populations. Newberry obsidian contains numerous clasts with round or ellipsoid bubbles, whereas irregular and collapsed bubble shapes are most common at Mono Craters (Fig. 14b). Furthermore, both the range and maximum H_2O content of Newberry obsidian pyroclasts are relatively constant throughout the eruption whereas at Mono Craters, with the exception of the initial bed (Herd 1994), there is a systematic decrease in both maximum and average H_2O contents with stratigraphic height. In addition, few analyzed obsidian clasts from Mono Craters have <0.5 wt.% water (Fig. 14), suggesting that obsidian clasts may have been sourced at a different depth range than Newberry. Finally, with the exception of clasts that contain xenoliths, CO_2:H_2O ratios are substantially lower in Newberry obsidian than in the Mono Craters sample suite.

The high CO_2:H_2O ratios of the Mono Craters obsidian pyroclasts has been a topic of debate (Dobson et al. 1989; Gonnermann and Manga 2005; Newman et al. 1988; Rust et al. 2004), as they are too high to be explained by the open-system degassing apparently required for obsidian formation. These CO_2:H_2O ratios are considerably greater than for the Newberry obsidian without xenoliths but are substantially lower than in many xenolith-bearing Newberry clasts. As we infer that the CO_2 enrichment of melt adjacent to xenoliths in NP samples results from heating of hydrothermal carbonate minerals, partial assimilation of xenoliths might also explain the high CO_2:H_2O ratios of the Mono Craters obsidian pyroclasts. Indeed, Mangan and Sisson (2000) found that after prolonged heating of Mono Craters obsidian dome samples with CO_2 contents below detection limit, the glass became homogeneously enriched in CO_2 (up to 62 ppm), and they concluded the CO_2 was derived from minute fractures dusted with carbonate. Although there is xenolith powder in obsidian pyroclasts from Mono Craters and every other suite that we have examined (Inyo volcanic chain and Little Glass Mountain CA, Rock Mesa and Cleetwood OR deposits; e.g. Wearn 2002; Rust et al. 2004), we have found no systematic difference between the volatile content of samples with or without xenoliths for any of these suites. Thus, xenoliths are unlikely to be a significant source of CO_2 in most obsidian pyroclasts, and the difference in CO_2: H_2O ratios for the xenolith-free clasts of the Newberry and Mono Craters eruptions is probably related to degassing conditions (original volatile composition of the magma and the extent of vapor fluxing).

The observed trend of decreasing maximum H_2O throughout the Mono Craters eruptive sequence has been interpreted as recording the shallowing of the fragmentation level through time (Newman et al. 1988). This model implies that episodic eruptions, with rapid downward migration of a decompression wave (e.g. Cashman and McConnell 2005), might involve fragmentation over a more extensive depth range than in steady eruptions (e.g., the Lower NP) where the depth of the fragmentation surface is balanced by relative rates of decompression and upward magma migration. If correct, we would expect to see similar evidence in late-stage obsidian pyroclastics from Newberry, where the presence of multiple ash layers suggests the onset of pulsatory activity. Instead, the maximum H_2O remains fairly constant. We conclude that differences in obsidian characteristics within and between eruptions are more likely to be related to processes of

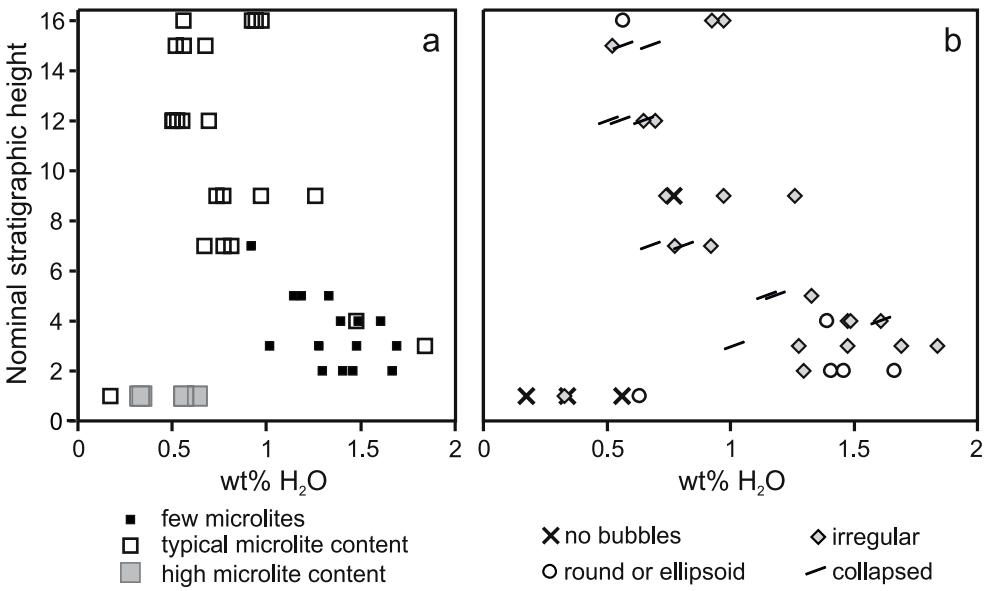

Fig. 14 Textures of obsidian pyroclasts determined from examination of samples collected by Herd (1994) from the Mono Craters 650 B.P. deposits. The *vertical axis* simply places samples in the stratigraphic sequence given in Newman et al. (1988). There are no data at stratigraphic heights 6, 8, 10, 11, 13 and14 because these represent units sampled by Newman et al. (1988) but not Herd (1994). **a** Relative microlite contents. **b** Bubble textures. Water contents are from our own measurements and differ slightly from those of Herd (1994)

magma intrusion and ascent, and contrasting plumbing geometries, than to conditions of fragmentation.

The data from Mono Craters and Newberry deposits as well as less extensive observations from other deposits (Castro and Mercer 2004; Rust 2003; Wearn 2002), suggest that there are systematic differences in the properties of obsidian from eruptions involving multiple, aligned vents (linked by a dike) versus single-vent eruptions. The available data indicate that high CO_2:H_2O ratios and abundance of obsidian may be signatures of shallow dike emplacement and large vapor fluxes through brecciated dike margins. By extension, the relative uniformity of obsidian produced during sustained single-vent eruptions may reflect integration of obsidian formed at different times and time scales within the conduit.

Conclusions

It has become standard to use pumice textures to infer eruption processes (e.g. Houghton and Wilson 1989; Klug et al. 2002; Mangan and Cashman 1996). However, not only are dense juvenile clasts rarely examined in detail (e.g. Cashman and Hoblitt 2004) but they are often classified as lithic clasts together with non-juvenile material (e.g., Kuehn 2002). Our study of clasts from the 1300 B.P. eruption of Newberry volcano shows that the abundance, textures, and H_2O and CO_2 contents of juvenile obsidian pyroclasts can vary substantially both within a single bed and throughout an eruptive deposit and can provide new information on magma ascent and eruption dynamics.

We interpret the ash layer between the Lower NP and Upper NP to mark a brief pause in explosive activity during which the upper conduit filled with magma. We find that obsidian in the Lower NP was derived mainly from magma in contact with wall rocks that was plucked out as the conduit widened, whereas obsidian at the base of the Upper NP represents fragments of degassed magma that plugged the conduit. This shift in the obsidian source is indicated by dramatic changes in the CO_2 content of glasses as well as changes in proportions of obsidian and lithic clasts in the deposit. In particular, almost all Lower NP obsidian clasts contain $\leq$6 ppm CO_2 and are black or grey (due to microlites). In contrast, CO_2 contents of obsidian from the Upper NP vary from undetectable to over 60 ppm and there are large fractions of clear obsidian, obsidian mingled with pumice, and obsidian with xenolith bands.

Destruction of a conduit plug at the start of the Upper NP produced the only fall deposit bed that contains more obsidian pyroclasts than lithic clasts. Both earlier and later in the eruptive sequence, obsidian, although an order of magnitude less abundant than lithic clasts, follows the same general pattern of increase and depletion as the lithic component. This shadowing of obsidian and lithic contents is most simply explained if the obsidian formed as dikes or veins in wall rock prior to erosion and incorporation into the eruption column with vent widening. This scenario also explains how obsidian pyroclasts with water contents indicative of shallow levels (e.g. 10s to 100s of meters) can be continuously entrained into the eruption column during steady eruptions such as the Lower NP and the Cleetwood eruption of Mount Mazama (e.g. Wearn 2002).

The maximum H_2O content of obsidian fragments remained approximately constant throughout the NP despite changes in eruption intensity and steadiness. It is unlikely that the fragmentation depth would remain constant with changes in eruption dynamics, particularly those related to plug formation and destruction. For this reason, we do not interpret the maximum H_2O content of obsidian clasts in the NP to reflect the fragmentation level in the conduit, although fragmentation depth certainly limits the maximum depth over which wall rock and included obsidian can be excavated during eruption. Instead, we conclude that the maximum H_2O contents of obsidian in the NP could reflect (1) the depths over which there is poorly vesicular, partially degassed magma (glass or molten proto-obsidian), or alternatively, (2) the maximum H_2O content for which obsidian is preserved (does not vesiculate) during decompression. The latter model relies on the delay time for bubble nucleation exceeding the quench time (a function of both H_2O content and magma viscosity) and has been used to explain formation of glass rinds on breadcrust bombs (Hoblitt and Harmon 1993; Wright et al. 2007).

We conclude that data on the H_2O and CO_2 compositions of obsidian pyroclasts provide limited constraints of the fragmentation level or the degassing mechanism of the bulk of magma erupted (i.e., pumice and ash). However, data on the proportions of total obsidian relative to lithic clasts, and on variations in the proportions of obsidian with distinct appearances, provide insights into changes in the dynamics of eruptions. Furthermore, pyroclastic obsidian gives unique information on magma ascent and degassing near conduit walls prior to (and possibly during) eruptions, as well as degassing and vapor flux in upper conduits prior to explosive clearing. Finally, both bubble shapes and volatile gradients preserved in pyroclastic obsidian provide constraints on time scales of magmatic processes that are not available through conventional physical volcanology approaches.

Acknowledgements This work was supported by NSF grants EAR-0207362 and EAR-0510437 to Cashman and NSERC and Royal Society URF fellowships to Rust. We thank P. Wallace and K. Wearn for interesting discussions, S. Kuehn for sharing his data, outcrops, and photos, R. Herd for access to his Mono Craters samples, and L. Carlson, L. Chitwood and the Bend/Fort Rock Forest Service for their help and permission to collect samples in the Newberry National Monument. The manuscript benefited from edits and reviews by J. McPhie, O. Spieler and another referee.

References

Bargar KE, Keith TEC (1999) Hydrothermal mineralization in GEO N-1 drill hole, Newberry volcano, Oregon. In: US Geol Surv Open-File Rep 86–44:1–18

Behrens H, Zhang Y (2001) Ar diffusion in hydrous silicic melts: implications for volatile diffusion mechanisms and fractionation. Earth Planet Sci Lett 192:363–376

Blank JG (1993) An experimental investigation of the behavior of carbon dioxide in rhyolitic melt. PhD thesis California Institute of Technology, Pasadena

Boudreau AE (1999) PELE—a version of the MELTS software program for the PC platform. Comput Geosci 25:201–203

Bursik M (1993) Subplinian eruption mechanisms inferred from volatile and clast dispersal data. J Volcanol Geotherm Res 57:57–70

Bursik M (2001) Effect of wind on the rise height of volcanic plumes. Geophys Res Lett 28:3621–3624

Carey S, Sparks RSJ (1986) Quantitative models of fallout and dispersal of tephra from volcanic eruption columns. Bull Volcanol 48:109–125

Carrigan CR, Eichelberger JC (1990) Zoning of magmas by viscosity in volcanic conduits. Nature 343:248–251

Cashman KV, Hoblitt RP (2004) Magmatic precursors to the 18 May 1980 eruption of Mount St. Helens, USA. Geology 32: 141–144

Cashman KV, McConnell SM (2005) Multiple levels of magma storage during the 1980 summer eruptions of Mount St. Helens, WA. Bull Volcanol 68:57–75. DOI 10.1007/s0045-005-0422-x

Castro JM, Mercer C (2004) Microlite textures and volatile contents of obsidian from the Inyo volcanic chain, California. Geophys Res Lett 31:L18605. DOI 10.1029/2004GL020489

Cioni R, Marianelli P, Santacroce R, Sbrana A (2000) Plinian and subplinian eruptions. In: Sigurdsson H, Houghton BF, McNutt SR, Rymer H, Stix J (eds) Encyclopedia of volcanoes. Academic Press, San Diego, CA, pp 477–494

Couch S, Sparks RSJ, Carroll MR (2003) The kinetics of degassing-induced crystallization at Souffriere Hills Volcano, Montserrat. J Petrol 44:1477–1502

Dobran R (2001) Volcanic processes: mechanisms in material transport. Kluwer, New York

Dobson PF, Epstein S, Stolper EM (1989) Hydrogen isotope fractionation between coexisting vapor and silicate glasses and melts at low pressure. Geochim Cosmochim Acta 53:2723–2730

Dunbar NW, Kyle PR (1992) Volatile contents of obsidian clasts in tephra from the Taupo Volcanic Zone, New Zealand: implications to eruptive processes. J Volcanol Geotherm Res 49:127–145

Eichelberger JC (1989) Research drilling in young silicic volcanoes. Sci Drill 1:90–102

Frost BR, Lindsley DHS (1992) Equilibiria among Fe–Ti oxides, pyroxenes, olivine, and quartz. 2. Aplication. Am Mineral 77:1004–1020

Gardner JE, Carey S, Sigurdsson H (1998) Plinian eruptions at Glacier Peak and Newberry volcanoes, United States: implications for volcanic hazards in the Cascade Range. Geol Soc Amer Bull 110:173–187

Gonnermann H, Manga M (2003) Explosive volcanism may not be an inevitable consequence of magma fragmentation. Nature 426:432–435

Gonnermann H, Manga M (2005) Nonequilibrium magma degassing: results from modeling of the ca. 1340 A.D. eruption of Mono Craters, California. Earth Planet Sci Lett 238:1–16

Hammer JE, Rutherford MJ (2002) An experimental study of the kinetics of decompression-induced crystallization in silicic melt. J Geophys Res 107:2021. DOI 10.1029/2001JB000281

Hammer JE, Cashman KV, Hoblitt R, Newman S (1999) Degassing and microlite crystallization during the pre-climactic events of the 1991 eruption of the Mt. Pinatubo, Phillipines. Bull Volcanol 60:355–380

Heiken G, Wohletz K, Eichelberger JC (1988) Fracture fillings and intrusive pyroclasts, Inyo Domes, California. J Geophys Res 93:4335–4350

Herd RA (1994) Degassing mechanisms during explosive volcanic eruptions. PhD thesis, Lancaster University, Lancaster

Hess K-U, Dingwell DB (1996) Viscosity of hydrous leucogranitic melts: a non-Arrhenian model. Am Mineral 81:1297–1300

Hoblitt RP, Harmon RS (1993) Bimodal density distributions of cryptodome dacite from the 1980 eruption of Mount St. Helens, Washington. Bull Volcanol 55:421–437

Houghton BF, Wilson CJN (1989) A vesicularity index for pyroclastic deposits. Bull Volcanol 51:451–462

Ihinger PD, Hervig RI, McMillan PF (1994) Analytical methods for volatiles in glasses. In: Carroll MR, Holloway JR (eds) Volatiles in magmas. Rev Mineral 30:67–121

Jaupart C, Allegre CJ (1991) Gas content, eruption rate and instabilities of eruption regime in silicic volcanoes. Earth Planet Sci Lett 102:413–429

Jensen RA, Chitwood LA (2000) What's new at Newberry Volcano, Oregon. In: Friends of the Pleistocene, PNW Cell Field Trip, pp 190

Keith TEC, Bargar KE (1988) Petrology and hydrothermal mineralogy of U.S. Geological Survey Newberry 2 drill core from Newberry Caldera, Oregon. J Geophys Res 93:10174–110190

Klug C, Cashman KV, Bacon CR (2002) Structure and physical characteristics of pumice from the climactic eruption of Mount Mazama (Crater Lake), Oregon. Bull Volcanol 64:486–501

Kuehn SC (2002) Stratigraphy, distribution, and geochemistry of the Newberry volcano tephras. PhD thesis, Washington State University, Pullman

Kuehn SC, Foit FF (2006) Correlation of widespread Holocene and Pleistocene tephra layers from Newberry Volcano, Oregon, USA, using glass compositions and numerical analysis. Quat Intl 148:113–137

Lange RA, Carmichael ISE (1987) Densities of Na_2O–K_2O–CaO–MgO–FeO–Fe_2O_3–Al_2O_3–TiO_2–SiO_2 liquids; new measurements and derived partial molar properties. Geochim Cosmochim Acta 51:2931–2946

Lange RA, Carmichael ISE (1990) Thermodynamic properties of silicate liquids with emphasis on density, thermal expansion and compressibility. In: Russell JK, Nicholls J (eds) Modern methods of igneous petrology; understanding magmatic processes. Rev Mineral 24:25–64

Lindsley DH, Spencer KJ (1982) Fe–Ti oxide geothermometry: reducing analyses of coexisting Ti-magnetite (Mt) and ilmenite (Ilm). Eos Trans AGU 63(18), Spring Meet Suppl, 471

Linneman SR, Myers JD (1990) Mafic magmatic inclusions in the Holocene rhyolites of Newberry Volcano, Oregon. J Geophys Res 95:17677–17691

MacLeod NS, Sherrod DR (1988) Geological evidence for a magma chamber beneath Newberry Volcano, Oregon. J Geophys Res 93:10067–10079

Mangan MT, Cashman KV (1996) The structure of basaltic scoria and reticulite and inferences for vesiculation, foam formation, and fragmentation in lava fountains. J Volcanol Geotherm Res 73:1–18

Mangan MT, Sisson T (2000) Delayed, disequilibrium degassing in rhyolite magma: decompression experiments and implications for explosive volcanism. Earth Planet Sci Lett 183:441–455

Newman S, Epstein S, Stolper E (1988) Water, carbon dioxide and hydrogen isotopes in glasses from the ca. 1340 A.D. eruption of the Mono Craters, California: constraints on degassing

phenomena and initial volatile content. J Volcanol Geotherm Res 35:75–96

Newman S, Lowenstern JB (2002) VOLATILECALC: a silicate melt-H_2O–CO_2 solution model written in Visual Basic for excel. Comput Geosci 28:597–604

Rust AC (2003) Viscosity, deformation and permeability of bubbly magma: applications to flow and degassing in volcanic conduits. PhD thesis, University of Oregon, Eugene

Rust AC, Manga M (2002) Bubble shapes and orientations in low Re simple shear flow. J Colloid Interface Sci 249:476–480

Rust AC, Manga M, Cashman KV (2003) Determining flow type, shear rate and shear stress in magmas from bubble shapes and orientations. J Volcanol Geotherm Res 122:111–132

Rust AC, Cashman KV, Wallace P (2004) Magma degassing buffered by vapor flow through brecciated conduit margins. Geology 32:349–352

Schlinger CM, Rosenbaum JG, Veblen DR (1988) Fe-oxide microcrystals in welded tuff from southern Nevada: origin of remanence carriers by precipitation in volcanic glass. Geology 16:556–559

Sieh K, Bursik M (1986) Most recent eruption of the Mono Craters, Eastern California. J Geophys Res:12539–12571

Smith JV (1996) Ductile-brittle transition structures in the basal shear zone of a rhyolite lava flow, eastern Australia. J Volcanol Geotherm Res 72:217–223

Sparks RSJ, Tait SR, Yanev Y (1999) Dense welding caused by volatile resorption. J Geol Soc (Lond) 156:217–225

Stasiuk MV, Barclay J, Carroll M, Jaupart C, Ratte C, Sparks RSJ, Tait S (1996) Degassing during magma ascent in the Mule Creek vent (USA). Bull Volcanol 58:117–130

Taylor BE (1991) Degassing of Obsidian Dome rhyolite, Inyo volcanic chain, California. Geochem Soc Spec Publ 3:339–353

Taylor BE, Eichelberger JC, Westrich HR (1983) Hydrogen isotopic evidence of rhyolitic magma degassing during shallow intrusion and eruption. Nature 306:541–545

Tuffen H, Dingwell DB, Pinkerton H (2003) Repeated fracture and healing of silicic magma generate flow banding and earthquakes? Geology 31:1089–1092

Watson EB (1991) Diffusion of dissolved CO_2 and Cl in hydrous silicic to intermediate magmas. Geochim Cosmochim Acta 55:1897–1902

Wearn KM (2002) Pyroclastic obsidian from the Cleetwood and Rock Mesa eruptions, Central Oregon. MSc thesis, University of Oregon, Eugene

Wilson CJN, Hildreth W (1997) The Bishop Tuff: New insights from eruptive stratigraphy. J Geol 105:407–439

Wright HM, Cashman KV, Rosi M, Cioni R (2007) Breadcrust bombs as indicators of eruption dynamics at Pichincha volcano, Ecuador. Bull Volcanol 69:281–300. DOI 10.1007/s00445-006-0073-6

Zhang Y, Behrens H (2000) H_2O diffusion in rhyolite melts and glasses. Chem Geol 169:243–262